

Unterschrift des Betreuers



DIPLOMARBEIT

Atmospheric contribution to decadal-scale polar motion variations from twentieth century reanalysis

Ausgeführt am Department für

Geodäsie und Geoinformation
der Technischen Universität Wien

unter der Anleitung von Prof. Dr. Johannes Böhm und Dr. Michael Schindelegger
als verantwortlich mitwirkendem Universitätsassistenten

durch

Matthias Aichinger-Rosenberger

Ried 14/7
6306 Söll

Datum

Unterschrift (Student)

Atmospheric contribution to decadal-scale
polar motion variations
from twentieth century reanalysis

Matthias Aichinger-Rosenberger

August 2015

Acknowledgements

At this point I want to express my thanks to all the people who helped me with the research and writing of this thesis and/or even beyond that made my whole academic career possible. At first and foremost to Dr. Michael Schindelegger, my supervisor who provided me an interesting topic, connecting geodetic science with my interest in atmospheric processes and helped me with a lot throughout the whole execution with my problems and misunderstandings. Secondly to all professors and assistants at TU Wien who's lectures I had the chance to hear, especially Dr. Johannes Böhm and Dr. Robert Weber for arousing my interest in higher geodesy. Furthermore a big thanks to my whole family, my parents in the first place, for giving me the opportunity to begin and finish my studies with their personal and financial support over the years.

Abstract

The origin of decadal variations in the excitation of polar motion occurs to be one of the remaining open questions in Earth rotation studies. Since William Markowitz discovered the multi-decadal wobble that has been named after him, geodetic science has been in search of the possible underlying physical mechanisms for it. Although a combination of different processes is the most likely scenario and most studies suggest processes in the core to account for the main contribution, a complete picture of the whole phenomenon is still missing. Atmospheric processes, although of subordinate magnitude, also take part in decadal polar motion excitation. The present study investigates this decadal-scale atmospheric excitation over the whole twentieth century by using meteorological data from two different reanalysis systems. On one hand the thesis estimates the atmospheric contribution to decadal-scale wobbles by comparing geophysical excitation measures to geodetic observations of polar motion variations. On the other hand two reanalysis models are tested for their rational skill and consistency through the angular momentum budget equation, i.e; the mathematical framework that is the foundation of a reliable estimation of the atmospheric contribution. In the end, a objective judgement on the usability of the reanalyses for Earth rotation studies is given, and the possible superiority of one of the probed datasets is pointed out. The atmospheric contribution is found to be small but not negligible. Beside that, good results in the angular momentum budget check justify the usage of both reanalyses models.

Kurzfassung

Der Ursprung von dekadischen Variationen in der Anregung der Polbewegung stellt eines der letzten großen Mysterien auf dem Gebiet der Erdrotation dar. Seit William Markowitz den multi-dekadischen Wobble entdeckte, welcher später nach ihm benannt wurde, versuchen Geodäten dessen Ursache auf den Grund zu gehen. Auch wenn heutzutage eine Kombination aus mehreren Prozessen am wahrscheinlichsten erscheint und die Prozesse im Erdkern wohl den Hauptanteil bilden so fehlt immer noch das vollkommene Verständnis für alle Zusammenhänge. Atmosphärische Prozesse stellen dabei auch einen kleinen Anteil dar. Diese Arbeit beschäftigt sich mit dem atmosphärischen Einfluss auf die dekadische Anregung der Polbewegung und bedient sich dabei meteorologischer Daten aus zwei verschiedenen Reanalysemodellen des 20. Jahrhunderts. Einerseits soll die Größenordnung des atmosphärischen Anteils geschätzt werden, andererseits werden im Zuge dieses Prozesses die verwendeten Modelle auf ihre Konsistenz und ihre Einsetzbarkeit in geophysikalischen Studien zur Erdrotation getestet. Schlussendlich soll damit eine objektive Bewertung möglich sein und eventuelle Vor- und Nachteile der einzelnen Modelle sollen aufgedeckt werden.

Contents

1	Introduction	6
1.1	Motivation	6
1.2	Scope of tasks	7
2	The Earth’s variable rotation	10
2.1	Precession	10
2.2	Nutation	11
2.3	Polar motion	12
2.3.1	Decadal polar motion	13
2.4	Length of day	16
3	Atmospheric excitation of Earth rotation	17
3.1	Angular momentum approach	17
3.2	Torque approach	23
3.2.1	Ellipsoidal torque	23
3.2.2	Mountain torque	24
3.2.3	Friction torque	24
3.3	Angular momentum budget	25
3.4	Pro and Contra of both approaches	27
4	Datasets	29
4.1	Meteorological data	29
4.1.1	NOAA CIRES Twentieth Century Global Reanalysis Version 2	29
4.1.2	ERA-20C Project	30
4.2	Geodetic data	30
4.2.1	IAU-2000 EOP 1846 – 2014	30

5	Practical Implementation	31
5.1	Data preparation	31
5.2	Computation of excitation measures	32
5.2.1	Topographic gradients	32
5.2.2	IB-correction for surface pressure	33
5.2.3	Torque computations	33
5.2.4	AAM computation	35
5.3	Filtering of time series	36
5.3.1	Unfiltered data	36
5.3.2	Removal of a composite cycle	38
5.3.3	Low-pass filtering	38
5.3.4	Running average filter	38
5.3.5	Test of filter methods	40
5.4	Comparison NOAA/ERA	41
5.4.1	Local torques	42
5.4.2	Ellipsoidal torque and AAM	45
5.5	Angular momentum budget check	49
5.5.1	Time domain	49
5.5.2	Frequency domain	57
5.6	Geophysical vs geodetic excitation	60
5.6.1	Time domain	60
5.6.2	Frequency domain	66
6	Discussion and final remarks	68

Chapter 1

Introduction

1.1 Motivation

The rotation of planet Earth appears to be no constant process. Both the orientation of the rotation vector with respect the mantle, as well as its magnitude, change on various time scales. In geodetic language usage we refer to these two phenomena as *polar motion* and changes in *length of day* (LOD). Both of them are caused by dynamic external and/or internal processes which are driven by the Sun, the Moon and other planets as well as the atmosphere, oceans, the outer and inner core and many other components. Of particular interest are decadal variations in polar motion, such as the Markowitz wobble, since their physical excitation mechanisms are still unknown.

Besides the fact that all of these variations can be observed with modern space geodetic techniques, one can also calculate the geophysical forcing caused by the atmosphere using data from numerical weather models and reanalysis systems. Basically there are two different approaches for explaining atmospheric excitation of the Earth's rotation, the *atmospheric angular momentum* (AAM) approach and the *atmospheric torque* approach. The availability of different models spanning the whole twentieth century allows an investigation even on multi-decadal variations in polar motion using the two approaches. A check of the angular momentum budget and a comparison to geodetic observations can be used for judging the rational skill of the specific model for Earth rotation studies. Although the likely influence of the atmosphere might be of subordinate relevance for decadal excitations, a

reliable estimation of its magnitude is a prerequisite for any future investigation on this subject.

1.2 Scope of tasks

The thesis deals with estimating the influence of the atmosphere on decadal variations in polar motion on the basis of meteorological data. In this case surface pressure and wind stress data are obtained from NOAA-20C, the NOAA (National Oceanic and Atmospheric Administration) CIRES Twentieth Century Global Reanalysis, and ERA-20C, the ECMWF (European Center for Medium-Range Weather Forecasts) Atmospheric Reanalysis of the 20th Century, two different reanalysis efforts which both span the whole twentieth century. In the following the two models/datasets will simply be referred to as ERA & NOAA. These data are used to compute key quantities for atmospheric excitation following both the AAM and the torque approach. Mathematically equivalent, they allow not only the estimation of the atmosphere-induced decadal excitation but also a judgement of the rational skill of the underlying models. Therefore two novel sets of atmospheric angular momentum and torque series are computed and a numerical verification of the angular momentum budget is carried out. Additionally a third set of NCEP (National Centers for Environmental Prediction) reanalysis data is added and compared with the others. Considering the more sophisticated nature of this model, it is used as a benchmark for the excitation measures of the other two. At last a comparison with geodetic observations should round out the picture of the atmospheric influence on Earth's wobbles on time scales from 2 to 50 years.

According to this outline the most important steps were:

- **Data preparation:** First, surface pressure and wind stress data as well as surface information of each model had to be downloaded. The grid used in this study had a spatial resolution of $2^\circ \times 2^\circ$ and a temporal resolution of six hours. Furthermore since errors occurred especially in the NOAA dataset, a correction of the grids had to take place in order to ensure a reliable implementation right from the start.
- **Computation of excitation quantities:**
 - The initial task was a basic calculation of topographic gradients

from the provided model heights. This was done in longitude and latitude direction as both are required for the torque computation.

- An IB-corrected Land-Sea mask was produced for modelling the oceanic response to surface pressure variations.
 - The three different torque components were computed by using the data from both NOAA and ERA over the period from 1900 to 2010. For the NOAA friction torque an external computation of the wind stress had to be done, as the surface drag variables are not provided by this model.
 - The AAM values, both for pressure and wind terms, were computed from the two models. A simple linear relationship was used to convert the ellipsoidal torque into the pressure term.
- **Filtering:** A low-pass filter was applied to all the time series in order to retain signals with decadal periods. A cut-off frequency of 1.5 years was chosen and additionally an estimation and removal of the yearly signal (composite cycle) took place. For visualization purposes, a running average filter was used, too.
 - **Comparison between NOAA/ERA in both time and frequency domain:**
 - First the results of the two models were compared using the filtered torque time series.
 - The second comparison was carried out on the basis of the filtered AAM terms. Here a third dataset (NCEP reanalysis) was used as a benchmark for the other two.
 - **AAM budget check:** A numerical verification of the AAM budget equation was carried out for both models. This gives information about their reliability when using them for Earth rotation studies. The budget was analysed both visually, by plotting the results, and statistically, by computing squared coherence and phase lag values in the frequency domain.
 - **Comparison to geodetic observations and interpretation:** Observations of polar motion variations from astrometry and space geode-

tic techniques were obtained in order to compare them to the atmospheric influence computed from the models in form of excitation measures. This confrontation illustrates the small but non-negligible atmospheric contribution to the excitation of polar motion variations on decadal time scales.

The first two chapters give some theoretical background that underlies the afore-mentioned tasks. Chapter 2 explains the main aspects of variations in the Earth's rotation, and Chapter 3 discusses their excitation by atmospheric processes, explaining the two available modelling methods. The practical implementation (Chapter 4 & 5) describes the preparation of data, the computations and utilized filtering methods used, as well as the key tasks of comparing the excitation measures to each other and to geodetic observations. The last chapter summarises the results and the scientific findings gained from it.

Chapter 2

The Earth's variable rotation

As already implied, the Earth's rotation is not constant over time. Changes in the rotational behaviour are described by using the Earth orientation parameters (EOP):

- **Precession-Nutation**
- **Polar motion**
- **Length of day or Universal Time**

Space geodetic techniques observe variations in all these parameters, in particular irregular fluctuations that can not be explained/modelled theoretically or empirically and have to be monitored instead. With Very Long Baseline Interferometry (VLBI) and Global Navigation Satellite Systems (GNSS) just the two most important systems should be mentioned here. The following sections include a short description of each EOP. Only polar motion will be discussed in more detail, especially its decadal variations as they are investigated throughout this thesis.

2.1 Precession

The basic physical consideration of precession is applying to the principle of a symmetric, but not spheric rotating spin-top. With an external force acting, the axis will move away in orthogonal direction. The figure of the Earth can be roughly approximated by a oblate spheroid, with the equatorial diameter being 43 km greater than the pole diameter. Gravitational forces acting on

the bulge cause a tilt-torque which tries to lift up the Earth's rotation axis. It evades this torque by a circular movement, describing a cone with an aperture angle of about 23.5° . This reaction is called precession movement in physics (Meschede, 2004 [17]). The whole set of gravitational forces on the Earth's spin movement can be subdivided into secular (precession) and periodic (nutation) effects.

2.2 Nutation

The cone figure of the rotation axis is not strictly maintained. Instead a nodding motion is described due to the overlapping of secular and periodic parts, i.e. the curve of a periodic function with its zero points on the precession circle. The principal term of nutation is due to the regression of the Moon's nodal line. It has a period of 18.6 years and reaches $\sim 6.8''$ in parallel and $\sim 9.2''$ in orthogonal direction to the ecliptic.

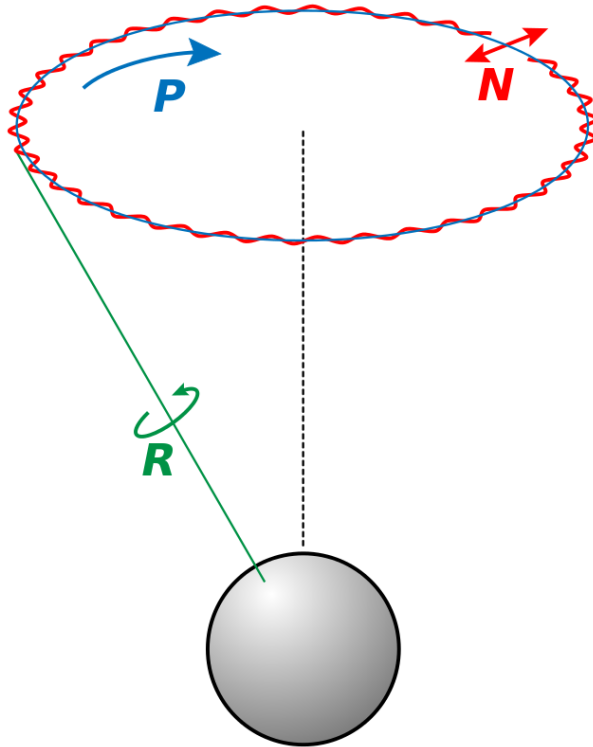


Figure 2.1: Precession and nutation, Source: commons.wikimedia.org, accessed: July 2015

2.3 Polar motion

The basic term polar motion comprises all motions of the solid Earth in relation to a space-fixed axis. For a terrestrial observer it manifests itself as a quasi-periodic motion of the pole attached to the Earth's rotation axis. If the Earth was completely rigid and spherical there would be no polar motion at all.

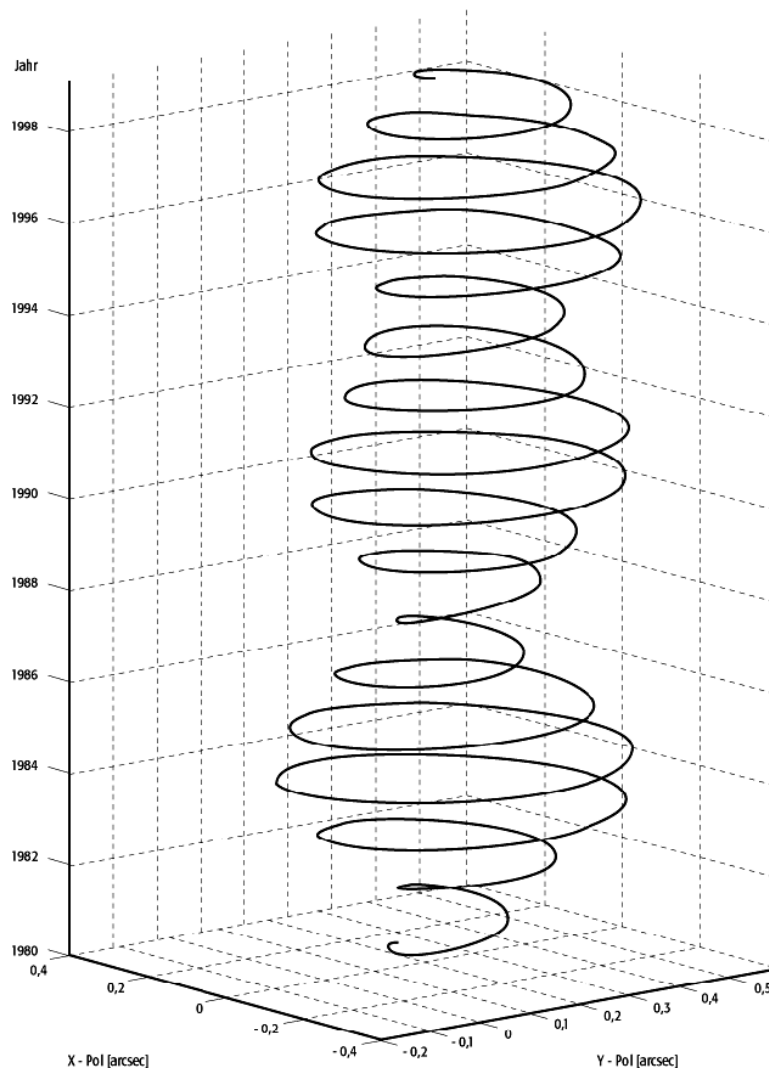


Figure 2.2: Polar motion from 1980–1998, Source: www.geodz.com, accessed: July 2015

In 1765, starting from the assumption of a rigid but oblate spheroidal Earth, Leonard Euler calculated a circular path of the pole with a period of 304 days. Based on astrometric observations by William Chandler in 1891, this calculation was shown to require refinement by taking into account the elastic properties of the Earth. This led to an oscillation with a period of 435 days which is generally reputed as the Chandler oscillation or Chandler wobble (CW). Additionally this free oscillation is superimposed by a forced component which is related to geophysical processes, whereas the free part is due to the fact that the rotation axis does not exactly match with the figure axis. Because of friction effects in the Earth’s interior, the Chandler oscillation is a damped oscillation which would vanish over time if there would be no recurring excitations. The exact excitation mechanism is still under investigation, even though nowadays there is broad consensus that the necessary energy to maintain the CW emerges from irregular processes in the atmosphere-ocean system (Gross, 2007 [13]).

2.3.1 Decadal polar motion

The excitation of polar motion variations on decadal timescales is still an unsolved issue among the geodetic community today. Since William Markowitz discovered the periodic signal (Markowitz, 1960 [16]), that was later named after him, geodetic science has been in search of a fully consistent explanation for it. Finding its main origin and the physical mechanism behind it appears to be a difficult task since many possibilities have proved to be incapable of providing the main excitation force. The following section gives an overview on today’s body of knowledge on the Markowitz wobble and the possible forces that could excite it, from atmospheric and oceanic processes to interactions between the interior parts of the Earth.

The Markowitz wobble

By analysing ILS (International Latitude Service) measurements from 1900 to 1959 William Markowitz found a component in polar motion, which he initially postulated as a periodic signal with an amplitude of 22 milliarcseconds (mas) and a period of 24 years. Later refinements in the description of the signal were done by Gross & Vondrak (1999 [11]), who, like Markowitz, used ILS data but combined it with other optical measurements, which led

to an extension of data by three decades compared to the original studies. These authors showed that the Markowitz wobble appears to be a not strictly periodic, but quasi-periodic motion, the amplitude of which ranges from 20 to 50 mas. The main excitation of this motion is still unknown today.

Possible origins for excitation: Atmosphere and ocean dynamics

Processes in the fluid layers of our planet cause variations in the Earth's rotation on many time-scales. This fact warrants the assumption that they might also influence decadal variations in polar motion. Picking up on these thoughts, Gross et al. (2005 [12]) performed an investigation on the redistribution of mass within the atmosphere and ocean system. Using AAM values from the NCEP Reanalysis and an Inverse-barometric (IB) approximation for modelling the ocean response to atmospheric forcing, they computed amplitudes of 9 mas (x -component) and 23 mas (y -component) which account for 20% (x) and 38% (y) of the observed excitation if expressed as ratios in peak-to-peak amplitudes (not considering phase and coherence relationships). Additionally they showed that the modelled atmospheric and oceanic excitation functions are barely significantly coherent and exhibit a likely out-of-phase behaviour with the observations. These points led to the conclusion that mass redistributions within the fluid layers are not capable of inducing the observed variations. The study of Gross et al. (2005 [12]) does not address the excitation of processes that change the total mass of the fluid layers, e.g ice masses input.

Wilson (1993 [29]) deduced that a decadal oscillation in the global sea level (GSL) due to the input of mass to the ocean would result in polar motion variations with a similar polarisation. Celaya et al. (1999 [3]) analysed the output of a coupled climate model, providing several interesting but also conflicting conclusions. They found that changes in the Antarctic snow pack and the ocean bottom pressure are capable of inducing decadal variations. However, these changes engender an implausible GSL, which has to rise up for nearly 15 centimetres to account for the observed excitation. Furthermore the inferred wobble amplitudes were two times weaker and the periods and phases were not consistent with the observations. Combining the results of all the mentioned studies leads to conclusion that atmosphere and ocean dynamics can only provide a small contribution to the entire

excitation process of decadal polar motion variations.

Core- mantle interactions

The first attempt for an explanation considering the interior parts of the Earth was based on the interaction between the mantle and the fluid outer core. This idea originates from the fact that these core/mantle interactions are the main cause of decadal LOD-variations and thus could drive polar motion variations as well. The two mechanisms that can account for the interactions are electromagnetic coupling and topographic coupling torques. Electromagnetic coupling was found two to three times and topographic coupling three to ten times too weak in magnitude by Greff Lefftz and Legros (1995 [10]). This lack of power in the core-mantle interactions prompted the inclusion of the inner core. When studying its influence one has to consider the phenomenon of torsional oscillations. A very simplified description of it would be a relative motion between the fluid outer core and the surrounding solid parts (inner core and mantle). It could have a possible influence on polar motion through generating a torque both at the Core-Mantle Boundary (CMB) and the Inner Core Boundary (ICB). This could change the rotation of the inner core and, once again working on the assumption of angular momentum balance, the polar motion of the solid Earth. The torque acting at the ICB is believed to be an electromagnetic one, which causes a so-called inertial coupling between outer and inner core. This may result in a tilting of the inner core's figure axis and thus a change of its rotation and a reaction of the solid parts (mantle). The first suggestion by Greiner-Mai (2000 [9]) was a tilting of 1° . Dumberry and Bloxham (2002 [7]) found that the required torque is produced by a fluid motion associated with torsional oscillations and that a tilt of only 0.07° is enough to explain the Markowitz wobble. A very similar study was done by Mound (2005 [18]) using almost identical model parameters but including a second choice of 1 year for the relaxation time, which proved to produce realistic results for LOD-variations and fluid velocities. Nonetheless, for polar motion, neither 100 years nor 1 year of relaxation time could provide a torque strong enough to account for the observed wobble. The resulting amplitudes were three times smaller (10^{17} Nm) than those required (10^{20} Nm), leading to a disagreement with Dumberry and Bloxham that results from the adoption of more realistic velocity differences across the ICB, see Mound (2005 [18]). Both studies agreed on the

fact that the relaxation time could greatly influence the torques generated at the ICB and thus decadal polar motion variations. Today there is still a great need for more sophisticated models of velocities, flow, and viscosity values within the core to obtain the chance of providing an explanation for the excitation mechanism behind the Markowitz wobble.

2.4 Length of day

Just as the orientation of the solid Earth's rotation axis, its magnitude (or angular speed) is also no constant quantity. The so-called excess length of day (LOD) is the common measure for the variations in the Earth's rotation rate. Through differentiation it can be computed from dUT1, the deviation of the mean world time UT1 (Universal Time) from the coordinated world time UTC (Universal Time Coordinated). The LOD-variations show many different periods, assigned to different geophysical processes. At daily and sub-daily periods the main excitation comes from ocean tides, while for periods of 14 to 28 days the tides of the solid Earth appear to be the major driving force. Due to tidal friction the angular speed decreases on secular periods, resulting in an increase in LOD of 1.8 ms per 100 years. Alongside those effects mentioned here, there are influences from the atmospheric and oceanic processes as well as the interior parts of the Earth. For instance interactions between the fluid outer core and the mantle were found to be the main excitation mechanism behind decadal LOD- variations.

Chapter 3

Atmospheric excitation of Earth rotation

Two different mathematical formulations can be applied to model the geophysical excitations of Earth rotation. The first one, known well as the angular momentum approach, represents the classical method for describing the effects of atmosphere and ocean dynamics based on the principle of angular momentum balance inside the system Earth. Alongside with that, a second, so-called torque approach, has gained importance over the last years. Also applying to the angular momentum balance, it explains rotational variations as a result of external torques caused by the fluid parts of the system acting on the solid Earth. Being analytically and physically equivalent, both should provide similar results (Schindelegger et al., 2013 [24]) and both of them are utilized in this study of decadal excitation in polar motion. For that reason this chapter shortly outlines the mathematical framework for both approaches. It mainly follows Schindelegger et al. (2013 [24]).

3.1 Angular momentum approach

As a consequence of Newtonian physics the angular momentum H of any isolated system is constant over time in absence of external forces (torques L) acting on it. This basic fact is represented by the motion equation of a rotating body

$$L = \frac{\partial H}{\partial t}. \quad (3.1)$$

When conducting studies on polar motion or LOD variations one has to rewrite it to

$$L = \frac{dH}{dt} + \omega \times H \quad (3.2)$$

due to the fact that the rotating reference system is attached to the body (Munk and MacDonald, 1960 [19]).

Assuming a rigid body, the angular momentum H can be written as the product of the tensor of inertia I and the angular speed Ω . However, in a realistic model of our planet, deformations have to be considered by introducing the relative angular momentum h

$$H = I\omega + h. \quad (3.3)$$

The tensor of inertia I represents the mass distribution inside the system and the relative angular momentum h describes their re-distribution relative to the rotating system (Schindelegger, 2009 [22]). Once again working on the assumption that H is constant in the absence of external torques, the instantaneous rotation vector ω has to vary both in magnitude and direction. A combination of (3.2) and (3.3) leads to the motion equation of a deformable body, the *Liouville equation*:

$$L = \frac{d}{dt}(I\omega + h) + \omega \times (I\omega + h). \quad (3.4)$$

The basic task now is to transform the equation into a form that can practically be used for studying Earth rotation in a geophysical sense. This can be done either by a linear analytical or a non-linear numerical approach. In the following the first method will shortly be explained here, for the non-linear approach further details can be found in Seitz (2004 [21]).

Considering the fact that the rotation of the solid Earth only marginally deviates from a steady-rotation initial state (subscript 0), a linearisation can be carried out. The system Earth including all solid and fluid parts is rotating with a constant mean angular velocity Ω around the z-axis of an Earth-fixed reference frame. The inertia tensor should become diagonal, thus z-axis and figure axis have to coincide, and the unperturbed rotation vector reads

$$\omega_0 = \Omega z \quad (3.5)$$

$$I_0 = \begin{pmatrix} A & 0 & 0 \\ 0 & B & 0 \\ 0 & 0 & C \end{pmatrix}, \quad (3.6)$$

where A, B and C are the equatorial and axial moments of inertia. The fluid layers (atmosphere and oceans) and their motion induce a deviation from the initial state through mass redistribution and relative particle motion, thus inertia tensor and angular velocity become time-dependent quantities

$$h = \begin{pmatrix} h_1 \\ h_2 \\ h_3 \end{pmatrix}, h_1 + ih_2 = \hat{h} \quad (3.7)$$

$$I(t) = I_0 + \Delta I(t) = I_0 + \begin{pmatrix} \Delta I_{11} & \Delta I_{12} & \Delta I_{13} \\ \Delta I_{21} & \Delta I_{22} & \Delta I_{23} \\ \Delta I_{31} & \Delta I_{32} & \Delta I_{33} \end{pmatrix} \quad (3.8)$$

$$\Delta \hat{I} = \Delta I_{13} + i\Delta I_{23} \quad (3.9)$$

$$\omega(t) = \begin{pmatrix} \omega_1 \\ \omega_2 \\ \omega_3 \end{pmatrix} = \begin{pmatrix} m_1(t) \\ m_2(t) \\ 1 + m_3(t) \end{pmatrix} \Omega. \quad (3.10)$$

The $m_i(t)$ are dimensionless quantities which describe the perturbation of the rotation vector in the Tisserand system, i.e, the Earth-fixed system with the axis z that minimizes \hat{h} throughout the mantle (Munk and MacDonald, 1960 [19]). As Figure 3.1 visualizes, m_1 and m_2 can be interpreted as the polar motion components of the rotation vector and m_3 as changes in LOD. Substituting the last two equations in the Liouville equation and neglecting small quantities leads to a system of differential equations

$$\begin{aligned} \frac{\dot{m}_1}{\sigma_r} + m_2 &= \psi_2 \\ \frac{\dot{m}_2}{\sigma_r} - m_1 &= -\psi_1 \\ \dot{m}_3 &= \dot{\psi}_3, \end{aligned} \quad (3.11)$$

with the Euler-frequency σ_r being the frequency of resonance of a rigid Earth. The ψ_i , the so-called *excitation functions* read (Munk and MacDon-

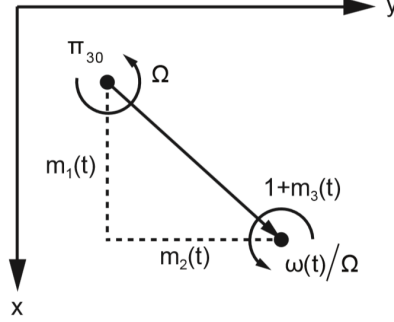


Figure 3.1: Perturbations of the instantaneous rotation vector $\omega(t)$ with respect to π_{30} , the figure axis of an undeformed Earth. Source: Schindelegger et al. (2013 [24])

ald, 1960 [19])

$$\begin{aligned}
 \psi_1 &= \frac{\Omega^2 \Delta I_{13} + \Omega \Delta \dot{I}_{23} + \Omega h_1 + \dot{h}_2}{\Omega^2 (C - A')} \\
 \psi_2 &= \frac{\Omega^2 \Delta I_{23} - \Omega \Delta \dot{I}_{13} + \Omega h_2 - \dot{h}_1}{\Omega^2 (C - A')} \\
 \psi_3 &= \frac{-\Omega \Delta I_{33} - h_3}{\Omega C},
 \end{aligned} \tag{3.12}$$

where ΔI_{i3} and h_i ($i = 1, 2, 3$) are the perturbations in the moment of inertia and the relative angular momentum, respectively, and A' is the average $(A + B)/2$, used to simplify the equations.

The fact that the axial component of (3.12) can be interpreted as an angular momentum whereas the equatorial components are torque-like terms, poses a problem for the evaluation of the differential equation system. The equatorial subset contains time-derivations of ΔI_{i3} and h_i , which cannot be obtained with sufficient accuracy from observations or atmospheric models. The solution is a partial integration of the excitation functions that leads to the definition of the *angular momentum functions* (Barnes et al. (1983 [1])). These once again can be split in axial and equatorial components and hence allow separate treatment of polar motion and variations in LOD. This

is accomplished by re-writing (3.12) to:

$$\hat{m} + \frac{i}{\sigma_r} \dot{\hat{m}} = \hat{\psi} = \hat{\chi} - \frac{i}{\Omega} \dot{\hat{\chi}} \quad (3.13)$$

$$m_3 = \psi_3 = -\chi_3 + \text{const.}, \quad (3.14)$$

with $\hat{\chi}$ and χ_3 being the equatorial and axial angular momentum functions:

$$\hat{\chi} = \chi_1 + i\chi_2 = \frac{\Omega\Delta\hat{I} + \hat{h}}{\Omega(C - A')} \quad (3.15)$$

$$\chi_3 = \frac{\Omega\Delta I_{33} + h_3}{C\Omega}. \quad (3.16)$$

All components now have angular momentum character, but the equations shown here are only valid for a non-deformable Earth, containing crust and mantle. Since this is not a valid model, small scaling factors that act as transfer ratios for a realistic Earth, have to be introduced. The following effects have to be considered (see Gross, 2007 [13] for a detailed discussion):

- Relative angular momentum of the core
- Rotational deformation
- Equilibrium pole tide
- Surface loading deformation
- Mantle anelasticity

With numerical values for the geodetic parameters given by Gross (2007 [13]), (3.15) and (3.16) can be written as

$$\hat{\chi} = \frac{1.100\Omega\Delta\hat{I} + 1.608\hat{h}}{\Omega(C - A')} \quad (3.17)$$

$$\chi_3 = \frac{0.748\Omega\Delta I_{33} + 0.998h_3}{\Omega C_m}. \quad (3.18)$$

Expression (3.17) is the actual version of equatorial angular momentum function that is used in this study. Its evaluation for the comparison with geodetic observations is described in Chapter 5. It should be noted here that this version is appropriate only for frequencies $\sigma \ll \Omega$. Investigations on short period excitations require adapted, frequency-dependent versions

of the equations presented here.

In a last step $\hat{\chi}$ and χ_3 can be split up in a *pressure* (or *matter*) term p , corresponding to the mass redistribution, and a *wind* (or *motion*) term w related to the relative angular momentum

$$\hat{\chi} = \hat{\chi}^p + \hat{\chi}^w \quad (3.19)$$

$$\chi_3 = \chi_3^p + \chi_3^w. \quad (3.20)$$

This subdivision also holds for the AAM components $H^{(a)}$ and reads

$$\hat{H}^{(a)} = H_1^{(a)} + iH_2^{(a)} = \hat{H}^p + \hat{H}^w \quad (3.21)$$

$$H_3^{(a)} = H_3^p + H_3^w. \quad (3.22)$$

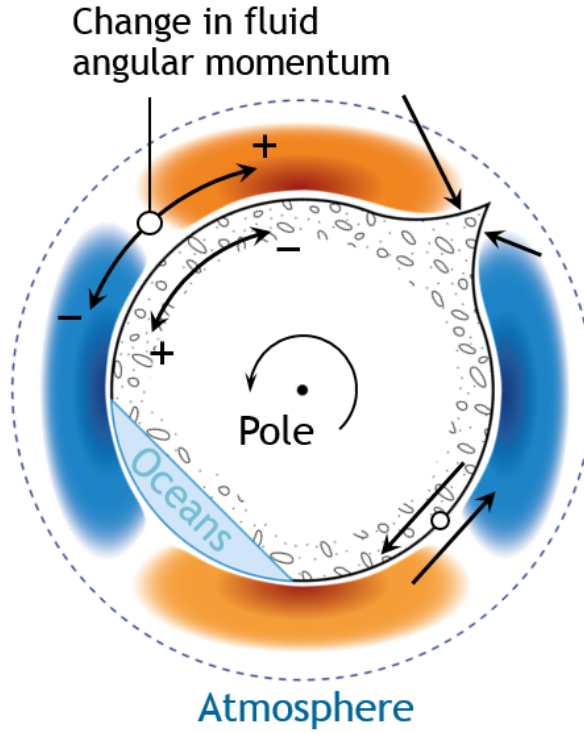


Figure 3.2: Illustration of angular momentum conservation (+/- arrows) in an Earth-fluid layer system as a pressure wave of two highs (orange areas) and two lows (blue areas) occurs in the atmosphere. Source: ggosatm.hg.tuwien.ac.at, accessed: July 2015

3.2 Torque approach

Besides the classical angular momentum approach, the influence of the atmosphere on the Earth rotation parameters can also be investigated by conceiving atmospheric forces as an external torque acting on the solid Earth. Analytically and physically equivalent to the AAM approach, it should produce the same results as the angular momentum approach. It can be applied to other fluid parts as well but since this thesis tackles the problem of atmospheric excitation, the focus here will be on the atmosphere.

The basic idea underlying the torque approach is the fact that every variation in the angular momentum of the solid Earth (s) is caused by atmospheric torques acting on it

$$L^{(a) \rightarrow (s)} = \frac{dH^{(s)}}{dt} \quad (3.23)$$

$$L^{(a) \rightarrow (s)} = -L^{(s) \rightarrow (a)} \quad (3.24)$$

$$\Rightarrow L^{(s) \rightarrow (a)} = \frac{dH^{(a)}}{dt}. \quad (3.25)$$

The total torque acting on the solid Earth (or the other way round on the atmosphere (a)) can be split into three components, which include the influence of pressure forces (p), friction drag (f) caused by surface winds and gravitational forces (g) (de Viron et al., 1999 [5])

$$L^{(s) \rightarrow (a)} = L^p + L^f + L^g. \quad (3.26)$$

As for the mathematical formulas of the components, only the equatorial parts are presented here, since the axial term is connected to LOD and not to polar motion variations.

3.2.1 Ellipsoidal torque

This component expresses the influence of the Earth's oblateness and its capability of inducing large pressure and gravitational torques on the atmosphere. It can be split into two constituents: a global one which is expressed by the Earth's form factor J_2 and a local one describing local anomalies of the geoid. Due to its small impact, the latter can be neglected at all frequencies. The remaining global component is labelled as the ellipsoidal or equatorial bulge torque (Schindelegger, 2014 [26]). Considering its connec-

tion to J_2 , it corresponds only to the spherical harmonic term of degree two/order one generated by the action of a global surface pressure field. This ellipsoidal contribution can once again be divided into a pressure term L^p and a gravitational term L^g , where the latter compensates about one half of the pressure term as shown by de Viron et al. (1999 [5]). Nonetheless, the sum of both is by far the most influential signal in the total equatorial torque. According to Wahr (1982 [27]) the ellipsoidal torque L^e is connected to the mass term of the equatorial angular momentum by a simple linear expression that uses only Ω as a scaling factor

$$\hat{L}^e = i\Omega\hat{H}^p. \quad (3.27)$$

3.2.2 Mountain torque

Similar to the L^p part of the ellipsoidal torque, the mountain torque also originates from pressure anomalies, but this time from local non-bulge topographic features. It is generated by a difference in surface pressure on the two faces of a mountain range, north-south oriented ranges like the Rocky Mountains or the Andes as well as east-west features like the Himalaya and in Greenland. The estimation of the mountain torque L^m can be accomplished by the multiplication of pressure values p_s with co-latitudinal (θ) and longitudinal (λ) gradients of orthometric height h and the mean radius of the Earth a . The exact mathematical expression reads

$$\hat{L}^m = a^2 \int \int p_s e^{i\lambda} \left(\frac{\partial h}{\partial \lambda} \cos\theta - i \frac{\partial h}{\partial \theta} \sin\theta \right) d\theta d\lambda. \quad (3.28)$$

3.2.3 Friction torque

The friction torque represents the friction force that is acting on the topography as a result of tangential wind stress in both zonal and meridional direction. The computation requires scalar fields for the friction force in both directions, which are a common output of most atmospheric models nowadays. In the absence of these data one has to derive equivalent scalar fields from ground-near winds, as it was done in this study for the NOAA model. The exact mathematical formulation is presented here

$$\hat{L}^f = -a^3 \int \int e^{i\lambda} (-\tau_\lambda \cos\theta + i\tau_\theta) \sin\theta d\theta d\lambda, \quad (3.29)$$

with $\{\tau_\lambda, \tau_\theta\}$ being the longitudinal (east) and co-latitudinal (south) components of the friction force acting on the solid Earth.

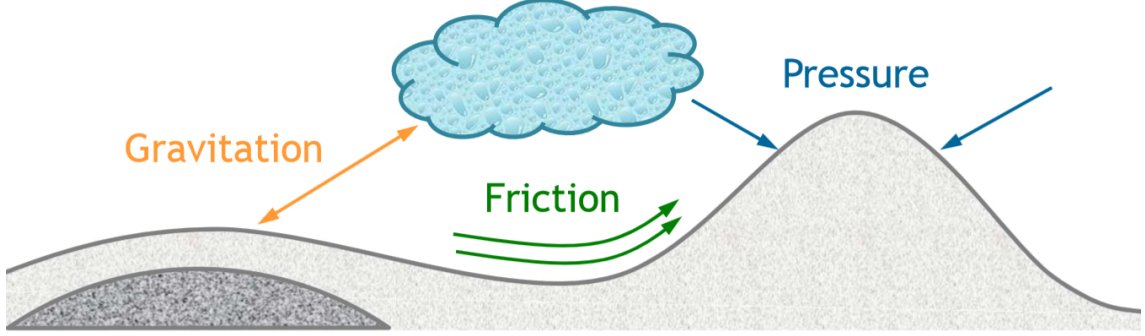


Figure 3.3: The different torque components, Source: Schindelegger et al. (2012 [23])

3.3 Angular momentum budget

The angular momentum budget is described by a simple differential equation that has been frequently tested in studies of Earth rotation variations using the torque approach. In vector-sized form it reads

$$\frac{d\hat{H}^{(a)}}{dt} + \Omega \times \hat{H}^{(a)} = \hat{L}^{(s) \rightarrow (a)} \quad (3.30)$$

The validations in different studies have shown that the time derivative of AAM can be indeed largely explained by interaction torques between the atmosphere and the solid Earth. This numerical equivalence mostly holds for long periods but vanishes at short time scales. Deviations between AAM derivative and torques are typically caused by the incompleteness of the utilized atmospheric models, in particular due to imperfect analysis data or parametrized fields, as noted by Schindelegger (2014, [26]). Of particular interest for this thesis is the equatorial part of the budget equation

$$\frac{d\hat{H}^{(a)}}{dt} + i\Omega\hat{H}^{(a)} = \hat{L}^{(s) \rightarrow (a)} \quad (3.31)$$

which can be expanded into its individual components:

$$\frac{d(\hat{H}^p + \hat{H}^w)}{dt} + i\Omega(\hat{H}^p + \hat{H}^w) = \hat{L}^e + \hat{L}^m + \hat{L}^f, \quad (3.32)$$

where $\{\hat{H}^p, \hat{H}^w\}$ denote the pressure/wind term of AAM and $\{\hat{L}^e, \hat{L}^m, \hat{L}^f\}$ the three torque components. Schindelegger et al. (2013 [24]) showed that the ellipsoidal part $\hat{L}^e = i\Omega\hat{H}^p$ is by far the largest part at seasonal time scales, providing $\sim 90\%$ of the whole signal. Thus, if the local torque components and the wind term cannot produce signals large enough to change this distribution, the AAM budget will be approximately closed per se.

This finding leads to the idea of evaluating a more sensitive budget version, the so-called residual budget equation, deduced by eliminating the bulge torque (i.e, pressure term) from the relationship

$$\frac{d(\hat{H}^p + \hat{H}^w)}{dt} + i\Omega(\hat{H}^w) = \hat{L}^m + \hat{L}^f. \quad (3.33)$$

This expression is largely governed by the local torques, and nearly the whole ellipsoidal part (except for the time-derivative) is left out of the equation. Through (3.33), one can mainly access how much of the wind term can be accredited to the torques.

The third version of the AAM budget analysed in this study tries to highlight the equivalence of the mountain torque and the wind term in (3.33) at low frequencies $\frac{d}{dt} \ll \Omega$

$$i\Omega\hat{H}^w \approx \hat{L}^m, \quad (3.34)$$

where the smallness of \hat{L}^f was implicitly assumed.

All three versions were used in Section 5.5 to gain information about the reliability and consistency of the different reanalysis efforts, thus laying the groundwork to answer one of the key questions of this thesis.

3.4 Pro and Contra of both approaches

This section summarizes the strengths and weaknesses of both approaches.

Angular momentum approach +

- The computation only needs surface pressure and three-dimensional wind data which are included in all available atmospheric analysis models.
- One has different choices for modelling excitation on different time scales, which means there are well-developed mathematical specifications of the approach at short and long periods.
- Due to the “average-like” calculation, the method is perceived as a robust one.

Angular momentum approach -

- Changes in the angular momentum caused by the atmosphere can only be detected, not attached to a certain process or phenomenon.
- The vertical integration over pressure levels requires large computational resources.

Torque approach +

- The approach gives clear information about the origin of the angular momentum changes as well as its spatial location.
- Only two-dimensional integrals have to be evaluated and thus the computational resources can be shortened.

Torque approach -

- An accurate computation requires high quality data from atmospheric models, surface variables at fine spatial resolution and parameters that are not directly observable. Furthermore, information on local land-air interactions (i.e the aerodynamic drag) is required.
- The mathematical framework connecting the torques to geodetic observations is not as sophisticated as for AAM and it is practically inappropriate for short periods.

- The approach is also inappropriate for modelling the excitation of nutation.

Chapter 4

Datasets

4.1 Meteorological data

This chapter gives a short description of the datasets that are used hereinafter. As already implied by the thesis title, all datasets span the whole twentieth century in order to be useful for this study. The first two sections present the very basic facts about history, assimilation methods, and products of the different reanalysis models. Most of the information given here is taken from the website of the CISL (Computational and Information Systems Laboratory) Research Data Archive (<http://rda.ucar.edu/>, accessed: July 2015). The third section describes the set of geodetic observations of polar motion used for the comparison in Section 5.6.

4.1.1 NOAA CIRES Twentieth Century Global Reanalysis Version 2

The Twentieth Century Reanalysis Project is an international effort to provide a global atmospheric reanalysis dataset (Compo et al., 2011 [4]) spanning the entire twentieth and about 30 years of the nineteenth century (1871 – near present). It is supported by the Earth System Research Laboratory Physical Sciences Division from NOAA and the University of Colorado’s Cooperative Institute for Research in Environmental Sciences (CIRES) and Climate Diagnostics Center and used resources of the National Energy Research Scientific Computing Center. The assimilation includes only surface observations of synoptic pressure, monthly sea surface temperature and sea ice distribution. By using an Ensemble Kalman Filter method the dataset

provides 6-hourly ensemble mean and spread fields on a $2^\circ \times 2^\circ$ global latitude-longitude grid. The present thesis used these mean fields of surface pressure and surface winds from 1900 – 2010 to compute the key quantities for atmospheric excitation of the Earth’s rotation.

4.1.2 ERA-20C Project

The ERA-20C (ECMWF Atmospheric Reanalysis of the 20th Century) is an outcome of the ERA-CLIM project and represents the first atmospheric reanalysis of the twentieth century by the ECMWF (Poli et al., 2013 [20]). Spanning from 1900 – 2010 it assimilates surface pressure and surface marine wind observations and was produced in 2014 in 6 weeks employing 22 parallel computation streams. The assimilation used the 24-hour 4DVar-analysis method, with a variational bias correction for surface pressure observations. The standard temporal resolution is 3 h except for the analysis data, where certain parameters are only available in 6 h intervals. The dataset was used as the second choice and compared to the NOAA model in this study.

4.2 Geodetic data

4.2.1 IAU-2000 EOP 1846 – 2014

The EOP C01 is the basic series of the IERS (International Earth Rotation and Reference Systems Service) spanning the entire twentieth century. It contains EOP given in the 1997 IERS system at 0.1 yr intervals (1846 – 1889) and 0.05 yr intervals (1890 – now). IAU-2000 stands for the present conventional nutation model that is implemented. The EOP set is regularly recomputed to take advantage of both the improvement of the various individual contributions and the refinement of the analysis procedures. The information here was taken from the IERS datacenter website (Bizouard & Gambis, 1999 [2]).

Chapter 5

Practical Implementation

This section follows the outline of Section 1.2 and describes the implementation of the physical and mathematical framework from Chapter 3, by using real meteorological data obtained from the reanalysis models. Besides the computation of AAM and torque values, their comparison both to each other as well as to geodetic observations is a major part of this study. This task is accomplished both numerically and visually and therefore a number of different filter methods were tested.

5.1 Data preparation

The reanalysis probed datasets were initially downloaded from the corresponding archives of NOAA and the ECMWF. Not all of the raw data seemed to be reliable at the first glance. This holds especially for the NOAA dataset, the grid of which had to be corrected for several shifts to ensure a correct utilization. Afterward this initial modification, $91^\circ \times 180^\circ$ grids in latitude and longitude for orthometric height, surface pressure and wind vectors were available. Unfortunately the NOAA records lack wind stress data and only contain horizontal ground-near winds in both spherical coordinate directions. This fact will be addressed later in this chapter as it has some bearing on the friction torque computation. The temporal resolution of the raw data was:

- NOAA: monthly mean grids for both pressure & winds
- ERA pressure: one grid at 0 UTC every third day

- ERA winds: 4-times-daily grids every third day, averaged to daily mean fields

The 6-hourly sampling in the ERA winds was due to two aspects:

1. At the time of the computations, monthly averages in the ERA archives were not available yet.
2. Aliasing effects from strong diurnal tides (S_1, P_1, K_1) had to be avoided. If only one field per month or 3-days interval is processed, tides are undersampled and produce spurious seasonal signals.

The 3-days interval ERA sampling was translated to monthly mean values, resulting in arrays of global grids with a time dimension of 1332 months.

5.2 Computation of excitation measures

Based on the homogeneously geo- and time-referenced datasets the computation of the excitation measures was tackled. The derivation of topographic gradients and an IB-correction to the surface pressure field were necessary pre-calculations, before monthly values for torques and AAM could be obtained over the time period from 1900 – 2010.

5.2.1 Topographic gradients

The gradient-field of the orthometric height h (not relative angular momentum here!) in both latitude/longitude direction is a necessary parameter for evaluating the global mountain torque. The derivation applied here used the method of central difference quotients

$$\left(\frac{\partial h}{\partial \theta}\right)_i = \frac{1}{2d\theta}(h_{i+1}(\theta, \lambda) - h_{i-1}(\theta, \lambda)) \quad (5.1)$$

$$\left(\frac{\partial h}{\partial \lambda}\right)_i = \frac{1}{2d\lambda}(h_{i+1}(\theta, \lambda) - h_{i-1}(\theta, \lambda)) \quad (5.2)$$

and had to be adopted at $\lambda = 0^\circ$ (Greenwich meridian) and $\theta = \pm 90^\circ$ (poles). The result were two $91^\circ \times 180^\circ$ grids for $\frac{\partial h}{\partial \theta}$ and $\frac{\partial h}{\partial \lambda}$ for each model. These grids were used in the mountain torque computation.

5.2.2 IB-correction for surface pressure

Given the lack of a dynamically coupled ocean model for the present study, the oceanic response to atmospheric pressure variations must be modelled by either the non inverse-barometric (non-IB) or the inverse-barometric (IB) response. The IB model implies that a rising atmospheric pressure results in a sea level depression or vice versa and the ocean bottom pressure stays spatially constant. For the non-IB model the sea level stays invariant, the atmospheric variations get transferred the ocean bottom and thus the pressure there increases. Especially for short-period variations (5 – 10 days or less) this non-IB model is common, whereas for longer time scales the IB-version is preferred. As the real oceanic response is difficult to address, these models are more or less just approximations that are far from perfect. This fact can still be considered as a major problem for investigations concerning the geophysical excitation of Earth rotation.

In the course of this study an IB-corrected pressure grid was calculated for every epoch by using the mean pressure over ocean

$$\bar{p}_0 = \frac{1}{A_{ocean}} \sum_{\theta} \sum_{\lambda} p_{ocean}(\theta, \lambda) dA_{ocean}, \quad (5.3)$$

where A_{ocean} indicates the total ocean surface area and p_{ocean} is the pressure distribution over the oceans. This field was combined with pressure data over land by using a inverted Land-Sea-mask with 1 representing sea areas and 0 land cells. The resulting distribution was used when computing the IB-version of the pressure term that is needed to infer ERP predictions. The non-IB version was used in the budget checks.

5.2.3 Torque computations

The three torque components were computed from both models by applying the formulas (3.9), (3.10), and (3.11) to the surface pressure (using the non-IB pressure field) and wind stress data. The integrals were evaluated as a double sum over every month from 1900.01 till 2010.12, resulting in 2 time series for x - and y -component of mountain, friction and ellipsoidal torque. For the NOAA model, wind stress data were not available and so a detour had to be taken for the friction torque. Ground-near winds were utilized to derive the wind stress estimates. The basic steps of this procedure are

outlined below.

Wind stress estimation

The approach that was applied here is based on the study of Foreman and Emais (2010 [8]). It uses the so-called drag coefficient C_D as the decisive proportionality factor when estimating wind stress over land and ocean using ground-near wind velocities. Instead of accepting the drag values recommended by Foreman and Emais (2010 [8]), a $2^\circ \times 2^\circ$ C_D -grid was calculated using test data from MERRA (Modern-Era Retrospective Analysis for Research and Applications) and a linear mathematical model that was applied to the friction velocities u_* (eastward) and v_* (northward)

$$\begin{pmatrix} u_* \\ v_* \end{pmatrix} = \sqrt{C_D} \begin{pmatrix} U \\ V \end{pmatrix} + b \quad (5.4)$$

with a constant parameter b that had to be calibrated using the C_D -grid and mean velocities (U, V) as well as wind stress fields (τ_E, τ_N) from MERRA (test month July 1984). The relationship between the velocities (u_*, v_*) and the wind stress fields following Hellerman (1983 [14]) reads

$$\tau_E = g\sqrt{C_D}u_*^2 \quad (5.5)$$

$$\tau_N = g\sqrt{C_D}v_*^2. \quad (5.6)$$

Due to differences in frictional behaviour, one has to distinguish at least between land and ocean areas. Hence, two separate parameters b_{land} and b_{ocean} and two different masks for C_D were used. The final equations for the wind stress in both directions read

$$\tau_E = [\rho_s(\sqrt{2C_D}|U| + b_{land})^2]M_{land} + [\rho_s(\sqrt{C_D}|U| + b_{ocean})^2]M_{ocean} \quad (5.7)$$

$$\tau_N = [\rho_s(\sqrt{2C_D}|V| + b_{land})^2]M_{land} + [\rho_s(\sqrt{C_D}|V| + b_{ocean})^2]M_{ocean} \quad (5.8)$$

where $[U, V]$ are the ground-near (10 m) wind velocities, $[M_{land}, M_{ocean}]$ are the masks for land/ocean areas and ρ_s is the density of the surface. The intersect parameters were determined by a manual calibration through visual regression analysis in MATLAB. The two final choices were $b_{land} = 0.06$ and $b_{ocean} = 0.1$. Figure 5.1 shows the result for the eastward-direction for ocean (top) and land (bottom).

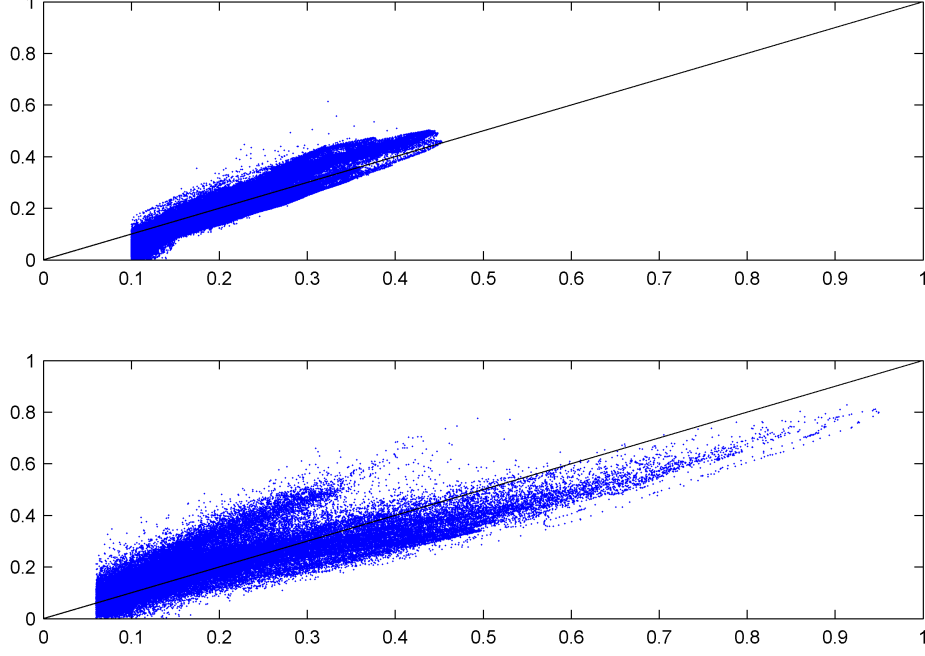


Figure 5.1: Manual calibration of the intersect parameter $b_{ocean} = 0.1$ (top) and $b_{land} = 0.06$ (bottom) in eastward direction. Label x -axis: $\sqrt{C_D}U$ (ocean) and $\sqrt{2C_D}U$ (land), y -axis: $\sqrt{\frac{\tau_E}{\rho_s}}$

In the last step the obtained wind stress components had to undergo a sign correction before they could finally be used in the evaluation of the friction torque (Schindelegger, 2014 [26]).

$$\tau_\lambda = \text{sign}(U)\tau_E \quad (5.9)$$

$$\tau_\theta = -\text{sign}(V)\tau_N. \quad (5.10)$$

5.2.4 AAM computation

The pressure terms can be computed in two different ways. The first one uses the strict mathematical formulation of \hat{H}^p

$$\hat{H}^p = -\frac{\Omega a^4}{g} \int \int p_s(\theta, \lambda) \cos \lambda + i \sin^2 \lambda d\theta d\lambda, \quad (5.11)$$

where g is the mean gravitational acceleration. For the discrete calculation the integrals are readily evaluated as double sums. The same pressure term results should be obtained by simply re-writing (3.27) to

$$\hat{H}^p = \frac{\hat{L}^e}{i\Omega}. \quad (5.12)$$

Comparing these two possibilities can only serve for testing the computational numerics. Since this was not a main point to be considered, this thesis forgoes a possible comparison.

The wind terms were evaluated by my supervisor Dr. Michael Schindlegger. The computation was quite time-consuming because, compared to the other excitation quantities, a third integration in the discrete vertical direction over n_p pressure levels had to be carried out. The mathematical expression for the wind term illustrates this fact:

$$\begin{aligned} \hat{H}^w = -\frac{a^3}{g} \int \int \left[\sum_{k=1}^{n_p} \frac{p_{k+1} - p_k}{2} \cos\lambda + i \sin\lambda [(u_k(\theta, \lambda) \right. \\ \left. + u_{k+1}(\theta, \lambda) \cos\theta + i(v_k(\theta, \lambda) + v_{k+1}(\theta, \lambda)))] \sin\theta d\theta d\lambda \right] \end{aligned} \quad (5.13)$$

where (u, v) are the winds (eastward & northward) on the different pressure levels. The AAM terms were now available, just as the torques, in form of a 1332 months-long time series for both models, spanning from January 1900 till December 2010. These were the series used in all following steps.

5.3 Filtering of time series

This section discusses the question of filtering the obtained time series: Why it was necessary even to apply a filter to the data, which filter was used for a certain application and what are the advantages/disadvantages of each one.

5.3.1 Unfiltered data

The unfiltered time series included signals of all different periods, the most dominant ones in the equatorial part being the annual- and the Chandler-period. Both of them, as well as the even shorter periods, were basically noise for the investigation of decadal variations. Figure 5.2 shows the dominant

parts of the annual wobble in the ERA- mountain torque (x -component) over the period of 25 years, approximately coinciding with that of the Markowitz wobble. In order to gain information about decadal variations in the time

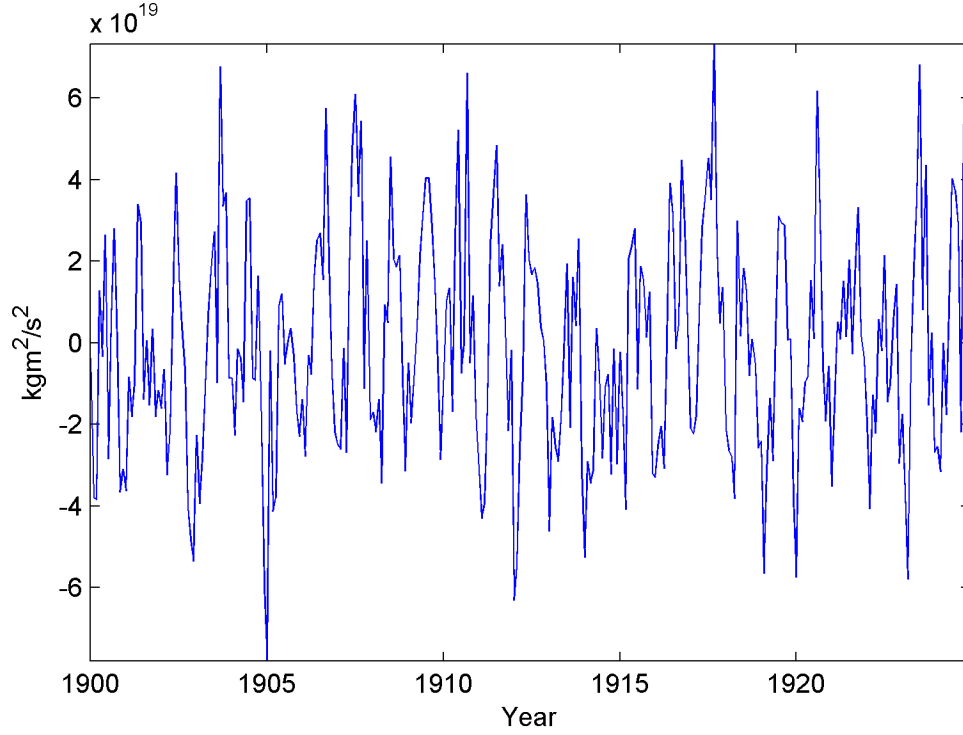


Figure 5.2: Unfiltered mountain torque x -component time series from 1900 – 1925 computed from ERA-data

series, the dominant annual wobble had to be removed. To achieve that, three different options were tested and combined:

- Removal of a composite cycle
- Low-pass filter
- Running average filter

5.3.2 Removal of a composite cycle

This method was used to remove the yearly signal $y(t)$ from the time series by estimating it as a periodic oscillation

$$y(t) = C_A \cos(\omega_a t) + S_A \sin(\omega_a t), \quad (5.14)$$

where ω_a is the angular frequency corresponding to one year. C_A and S_A are the unknown harmonic parameters which can be estimated through a simple least-squares adjustment using the computed signal as the observations. Then the yearly signal can be composed and removed from the computed time series. This adjustment was carried out and the signals were removed, resulting in a series that still included noise in form of the Chandler wobble and signals with periods shorter than one year. In order to get rid of them as well, an additional low-pass filter had to be applied.

5.3.3 Low-pass filtering

A Butterworth filter was used for the low-pass filter. The important parameters of it are its order and the cut-off frequency. The higher the order the more precise the filtering, but on the other hand high orders are likely to create artefacts at the start/end of the time series. After some testing, a filter of order three was applied to the data. The result of the combination of a low-pass filter and the composite cycle removal can be seen in Figure 5.3, where a cut-off frequency of 0.75 cpy (cycles per year) was used. Compared to Figure 5.2 the effects of the filtering are readily apparent.

All the torques and AAM terms of both models were low-pass filtered in this way. The resulting time series built the foundation for the evaluation of the AAM budget and the geophysical excitation functions in the comparison with geodetic observations.

5.3.4 Running average filter

In order to gain a clearer visualization of the torque and AAM comparison in the time domain, a running average filter was used. This method, also called moving average, is a type of convolution that can serve as an alternative for a low-pass filter in signal processing. It computes the mean over a given

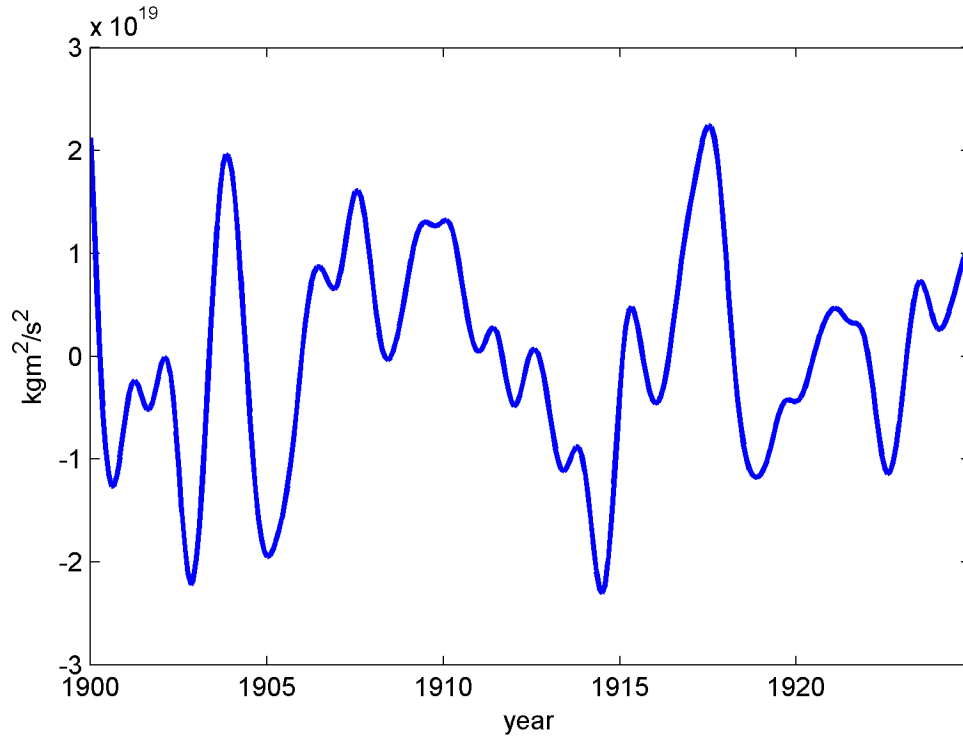


Figure 5.3: Mountain torque x -component time series from 1900 – 1925 computed from ERA data, low-pass filtered and with composite annual cycle removed

time window and sets it as the value of the first point in time. Then the window is shifted one value and the computation starts anew, resulting in the filtered value of point in time two. This process is continued throughout the whole time series.

The aim in using this type of filter here was to create a smoothing of the data, which gives a clearer visualization compared to the common low-pass filter. A window length of 24 months was used for all evaluations. Figure 5.4 shows the different outputs of a running average- and a low-pass filter for NCEP AAM data, in this case the y -component of the pressure term for 1948–2010.

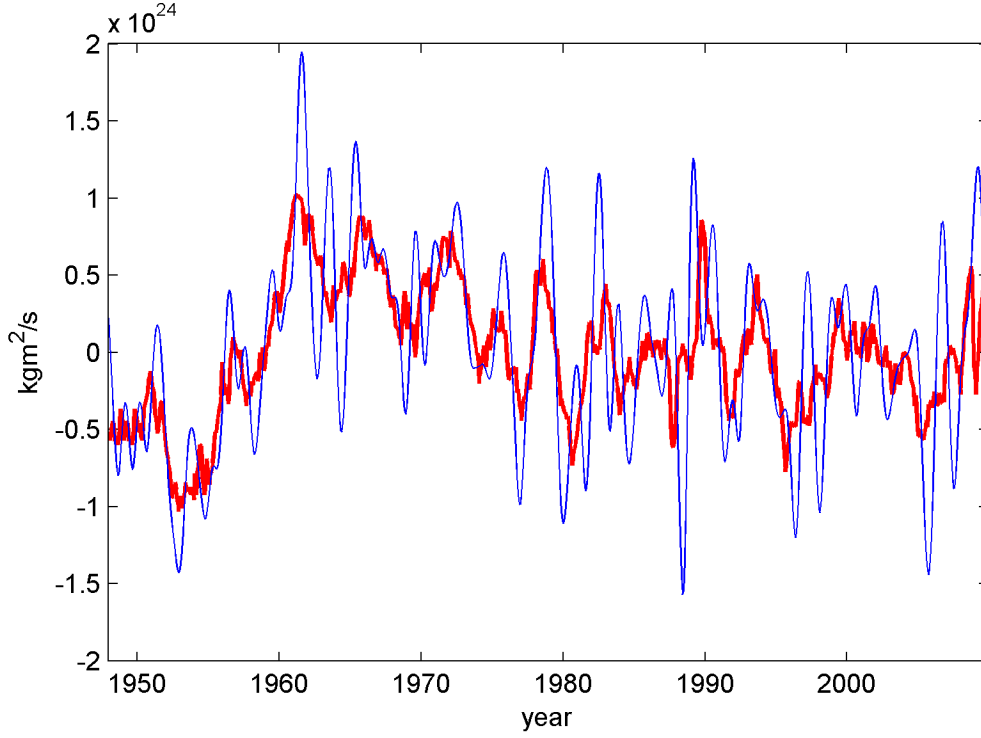


Figure 5.4: Comparison of a running average filter (red) to a common low-pass filter (blue) on NCEP AAM data: pressure term y -component

5.3.5 Test of filter methods

An important task when using filter methods on data is the clarification that the filter works the right way. In the frame of this study this means all signals with periods of 1 year and shorter should vanish from the data as well as possible. To verify that, long time series were mapped to the frequency domain and inspected visually. An example plot can be seen in Figure 5.5. It shows the successful filtering for the pressure term x -component of the NOAA time series. As apparent, noise in form of the short periods mentioned above, has been erased from the dataset. This test was made with all computed series, making sure that all of them were filtered the right way and were usable for the problem at hand.

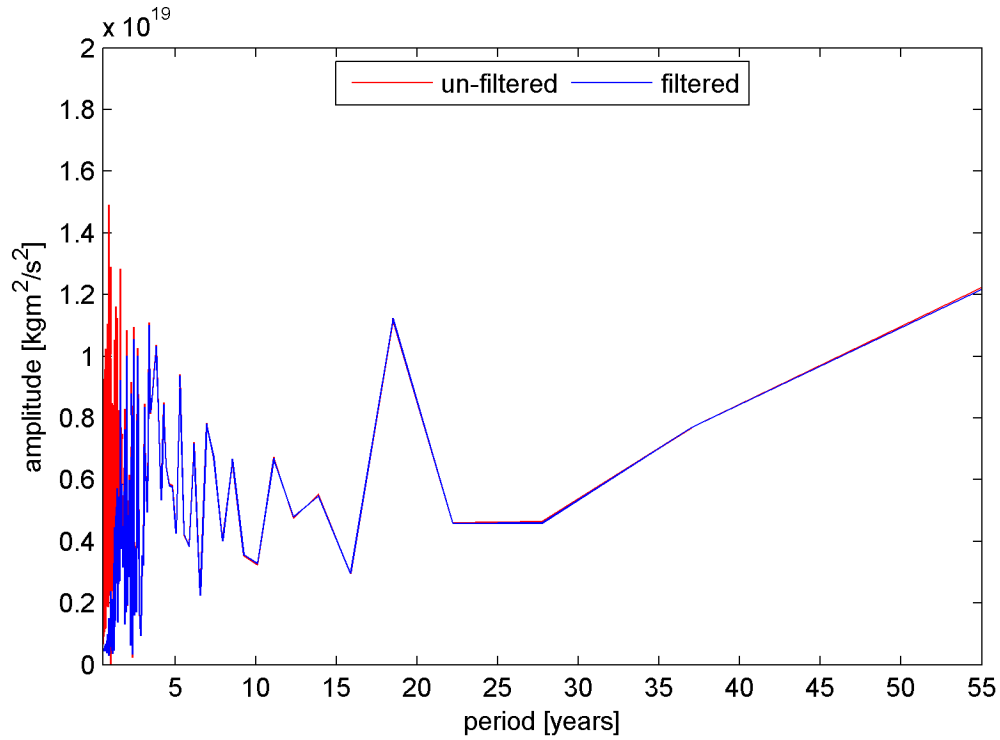


Figure 5.5: Comparison un-filtered vs filtered ellipsoidal torque NOAA x -component

5.4 Comparison NOAA/ERA

Drawing a comparison between torque and AAM values obtained from the ERA and NOAA datasets appeared to be the first key point in the course of this study. Through the visual inspection in time and frequency domain a first hint of the consistency of both efforts was gained. All the visualisations and statistics of this comparison are similar to the analysis of De Viron et al. (2004 [6]), who also used the NCEP/NCAR reanalysis as well as data from a 100-year run of the Hadley Centre general circulation model. Note that all the time series shown here were already filtered with the running average method as explained in Section 5.3 and the standard deviations are given in the unit of the corresponding quantity (angular momentum, torque, etc.)

5.4.1 Local torques

Mountain torque

Figure 5.6 representing the mountain torque series shows large similarities of both models over certain periods but not over the whole century, as indicated by the correlation values for the mountain torque in Table 5.1. In general the y -component matches better for both efforts than the x -component. In the period up from 1960 onwards, the two series show a very high correlation compared to the previous decades, a fact that can be linked to the build-up of a ground-based global network of observations in the 1950/60's. At the start of the twentieth century the data is represented mainly by surface and marine pressure observations. Despite the fact that the quality as well as the distribution of pressure observations is weak in the early twentieth century compared to later periods, the visualization shows remarkably good results, especially in the x -component from approximately 1910 up to 1940.

Compared to the study of De Viron et al. (2004 [6]), the mountain torque shows much better results for both components. This finding is derived by both visual and statistical comparison (Figure 5.6 & Table 5.1).

Table 5.1: Standard deviation [$\frac{\text{kgm}^2}{\text{s}^2}$] and correlation for ERA/NOAA: Local torques

	σ_x	σ_y	C_x	C_y
Mountain torque	6.29×10^{18}	4.35×10^{18}	0.77	0.51
Friction torque	2.01×10^{18}	1.95×10^{18}	0.33	0.29

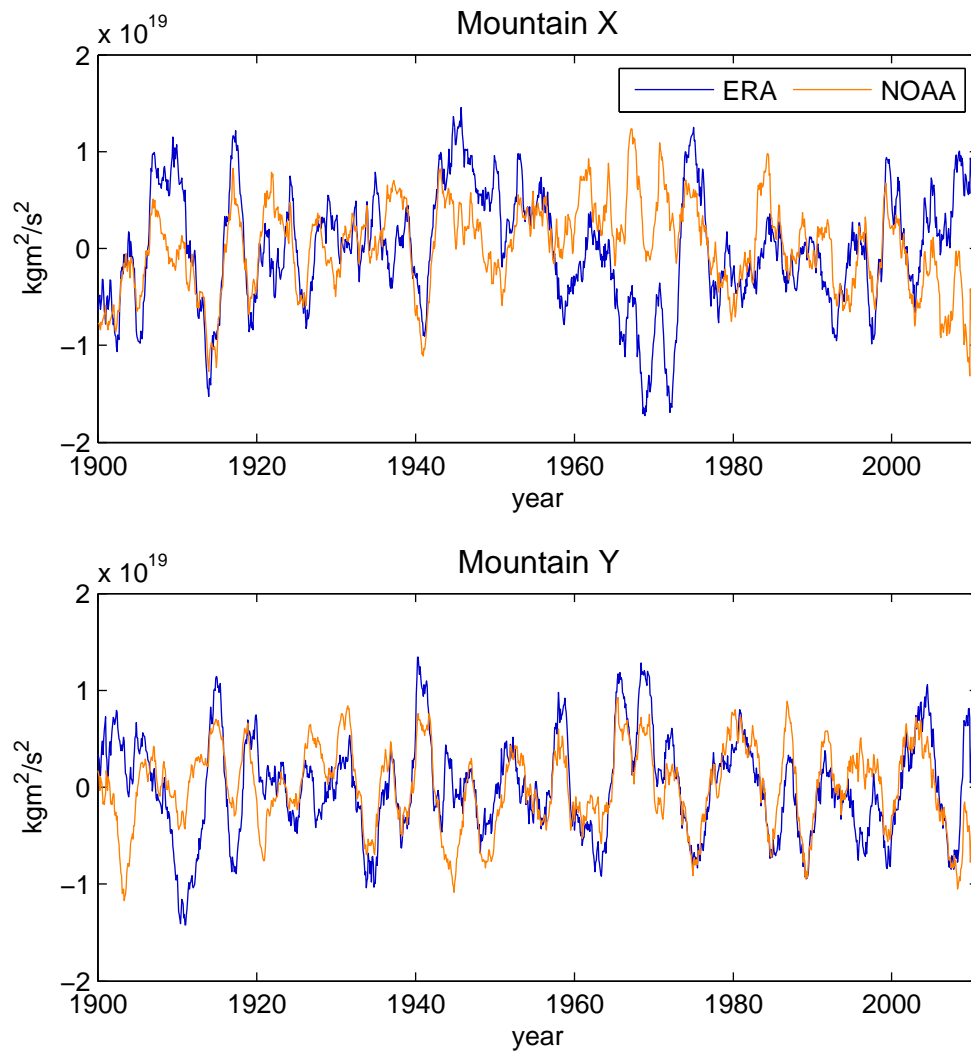


Figure 5.6: Mountain torque computed for ERA and NOAA data. Both time series are filtered with a running average filter, detrended and with a seasonal cycle removed

Friction torque

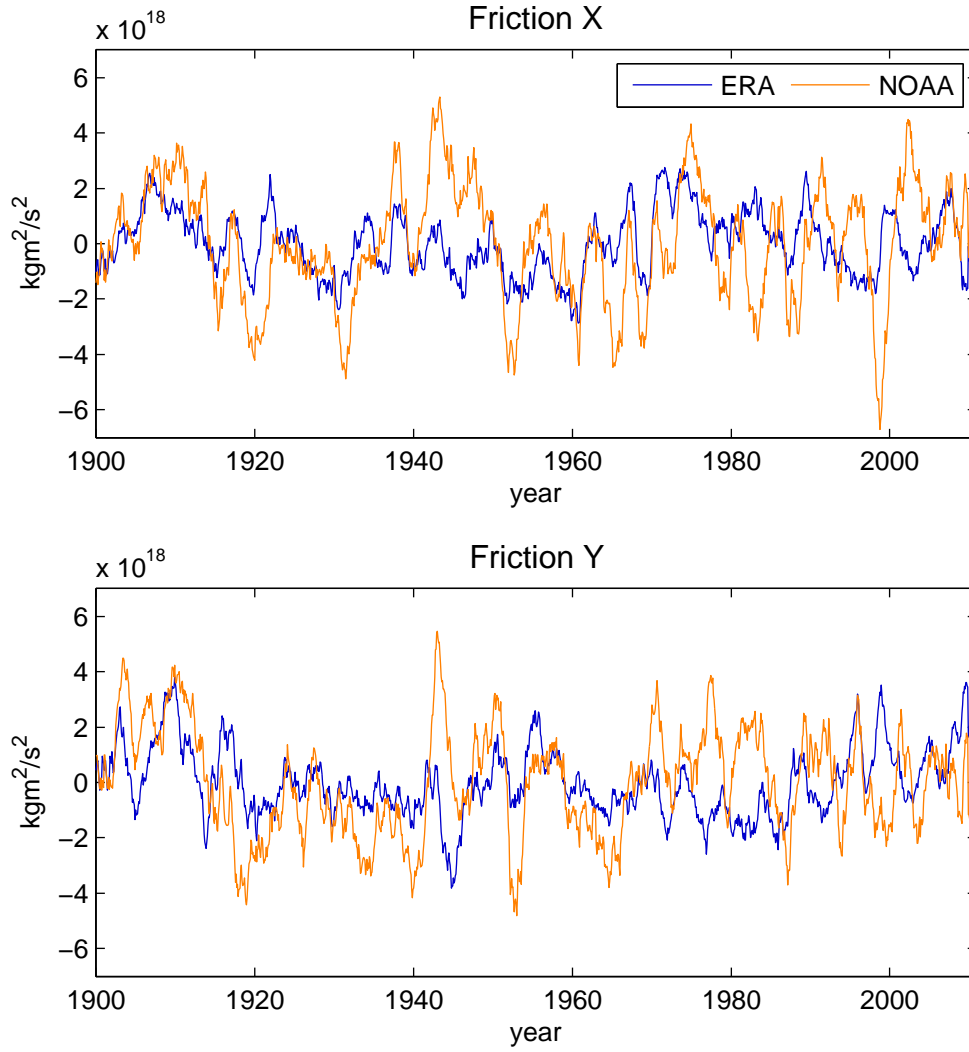


Figure 5.7: Friction torque computed for ERA and NOAA data. Both time series are filtered with a running average filter, detrended and with a seasonal cycle removed

The friction torque, shown in Figure 5.7, provides considerably worse results than the mountain torque in terms of correlation between NOAA and ERA, see Table 5.1. Despite this fact, the standard deviations are markedly lower

than for \hat{L}^m , due to the fact that the friction torque is approximately a factor of 3 smaller in magnitude than the mountain torque. The low correlation can be attributed to the external (and likely less accurate) computation of the surface stress for the NOAA model, outlined in Section 5.2.3. Visually and statistically, the coherence between ERA and NOAA in both components is somewhat inferior when compared to agreement achieved by de Viron et al. (2004 [6]) between the friction torques from the Hadley centre data and the NCEP reanalysis.

5.4.2 Ellipsoidal torque and AAM

Following the comparison of the local torque components the same procedure was carried out for the ellipsoidal part and the AAM wind term. The pressure term is left out here because of its linear relationship to the ellipsoidal torque. Both ellipsoidal torques and wind terms of ERA and NOAA were compared from 1900 – 2010. Additionally a third dataset, the NCEP/NCAR reanalysis I from 1948 – 2009 (Kalney et al., 1996 [15]), was used. Since it is assumed to be the most advanced of the three models, due to the inclusion of remotely-sensed and other conventional meteorological observations, it served as a benchmark for the other two. This could be helpful when tackling the question which one of the twentieth century reanalyses is the more reliable one.

Ellipsoidal torque

Figure 5.8 shows the ellipsoidal torque, which reaches the best match (combining x - and y -component) between the two reanalyses models. This is very likely attributed to the fact that the surface pressure is the main parameter in its calculation. Surface pressure observations are the observational core components of the reanalysis models tested here. Besides this fact, the good match for the mountain torque over specific periods also indicates that both models provide surface pressure data of approximately the same quality.

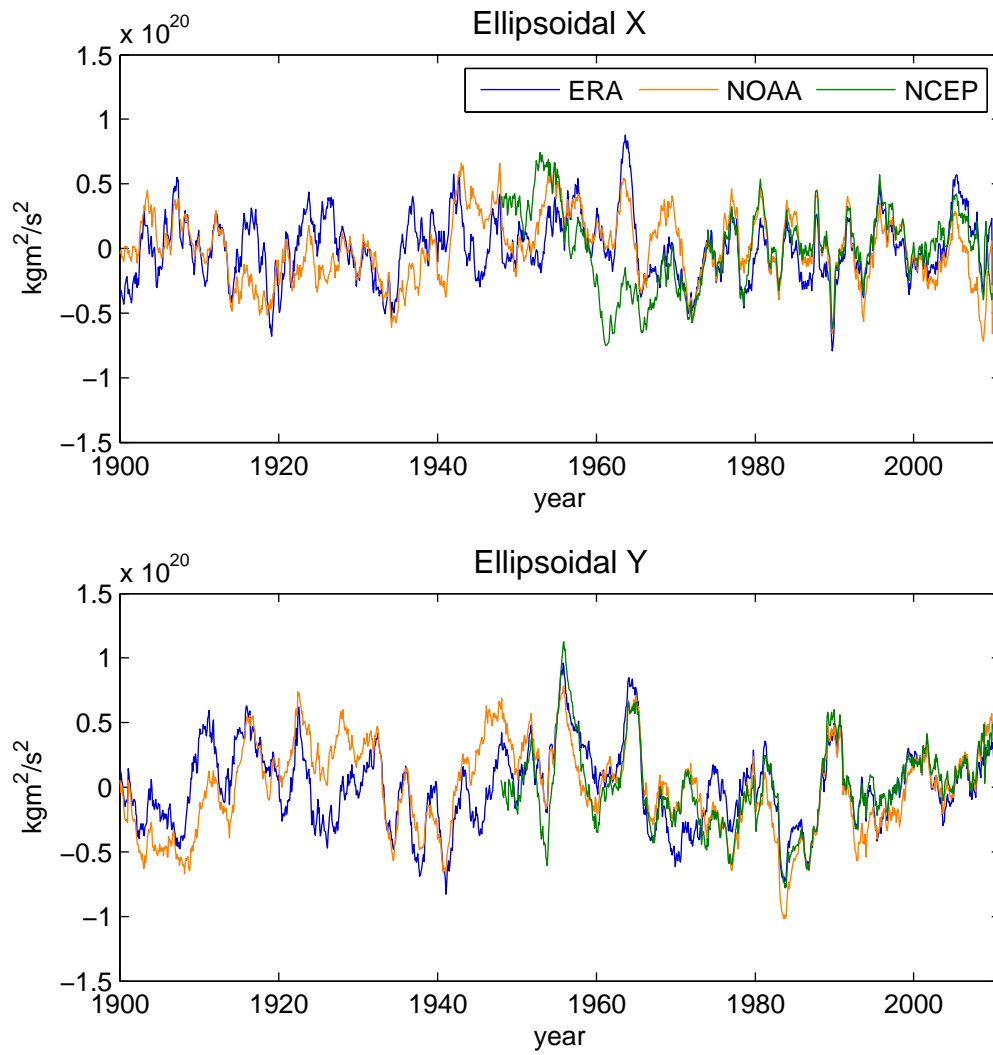


Figure 5.8: Ellipsoidal torque (non-IB) computed for ERA and NOAA data. Both time series are filtered with a running average filter, detrended and with a seasonal cycle removed

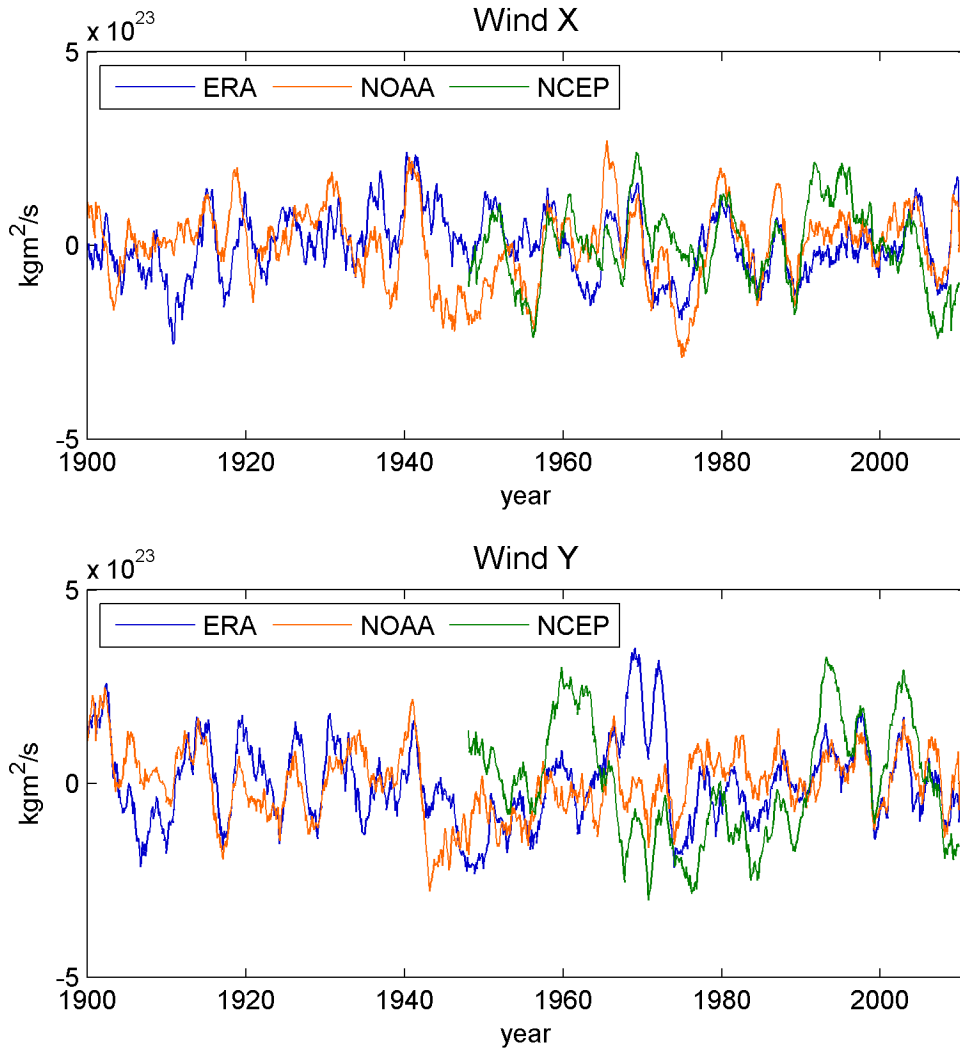


Figure 5.9: Wind term computed for ERA, NOAA and NCEP (1948 – 2009) data. The time series are filtered with a running average filter, detrended and with a seasonal cycle removed

The wind term (Figure 5.9 & Table 5.2) also shows periods of high correlation but in general weaker results than the pressure (ellipsoidal) terms which is likely related to the suboptimal vertical wind level data in the models, especially for the NOAA model, see Compo et al. (2011 [4]). This also shows in the comparison with the more sophisticated NCEP/NCAR

reanalysis.

Table 5.2: Standard deviation [$\frac{\text{kgm}^2}{\text{s}^2}$ (ellipsoidal torque) & $\frac{\text{kgm}^2}{\text{s}}$ (wind term)] and correlation ERA/NOAA: Ellipsoidal torque and wind term

	σ_x	σ_y	C_x	C_y
Ellipsoidal torque	2.28×10^{19}	2.52×10^{19}	0.96	0.90
Wind term	1.00×10^{23}	1.01×10^{23}	0.44	0.51

Table 5.3: Standard deviation [$\frac{\text{kgm}^2}{\text{s}^2}$ (ellipsoidal torque) & $\frac{\text{kgm}^2}{\text{s}}$ (wind term)] and correlation with NCEP series: Ellipsoidal torque and wind term

	σ_x	σ_y	C_x	C_y
Ellipsoidal torque ERA	3.05×10^{19}	1.66×10^{19}	0.96	0.93
Ellipsoidal torque NOAA	2.70×10^{19}	1.62×10^{19}	0.97	0.95
Wind term ERA	1.09×10^{23}	1.74×10^{23}	0.57	0.34
Wind term NOAA	1.02×10^{23}	1.52×10^{23}	0.57	0.37

As the correlation and standard deviation values in Table 5.3 indicate, there is a good match of both ERA and NOAA with the NCEP/NCAR reanalysis. This once again, holds particularly for the ellipsoidal torque whereas the wind term shows a bit weaker results. Tackling the question of superiority of ERA or NOAA, it is not possible to draw a clear conclusion from these statistics due to the fact that they are very similar for both models. In comparison to the study of De Viron et al. (2004 [6]) the results in both the visual and statistical analysis are much better for the ellipsoidal torque (pressure term) as the correlation with the NCEP/NCAR series is ~ 1.0 for both models and components, whereas those of De Viron et al. (2004 [6]) are ~ 0.0 . For the wind term, the differences are not huge, with the x -component being a little better and the y -component a little weaker for both ERA and NOAA than for the Hadley centre data in terms of correlation.

5.5 Angular momentum budget check

The evaluation of the angular momentum budget equation is a common method in studies of Earth rotation variations (de Viron et al., 1999 [5]). Basically its aim is to show the mathematical and physical consistency of the angular momentum and the torque approach. Knowledge about the level of this consistency can be useful when making a statement about which model provides better prerequisites for geophysical studies on the Earth's rotation. The three versions of the AAM budget, already outlined in Section 3.3, were tested for both reanalysis efforts. The first two parts were once again compared to the investigation of de Viron et al. (2004 [6]).

5.5.1 Time domain

Full budget

The full version of the angular momentum budget is the evaluation of equation (3.32), including the ellipsoidal parts (non- IB pressure term and ellipsoidal torque). As already mentioned in Section 3.3 one can expect the budget to be well closed at its full version. The results of the evaluation for ERA and NOAA can be seen in Figure 5.10 and Figure 5.11

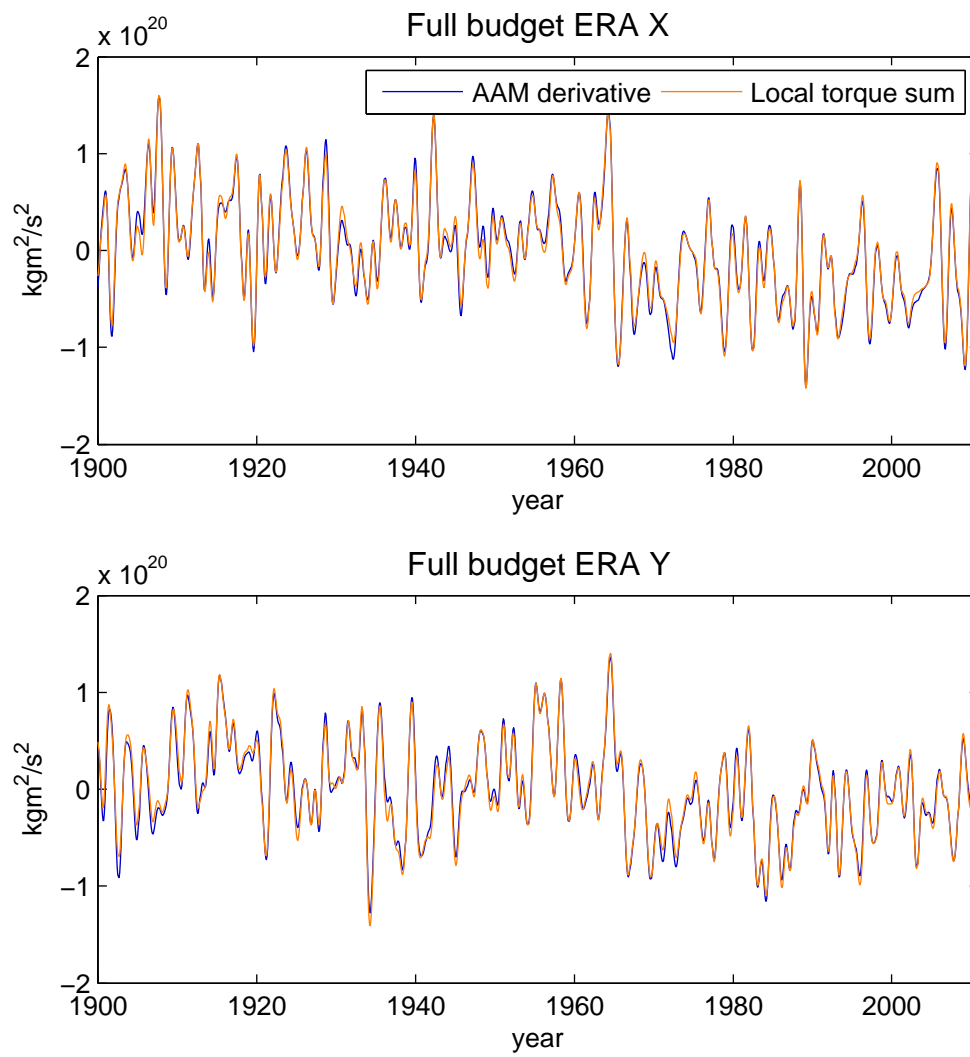


Figure 5.10: Full angular momentum budget of ERA

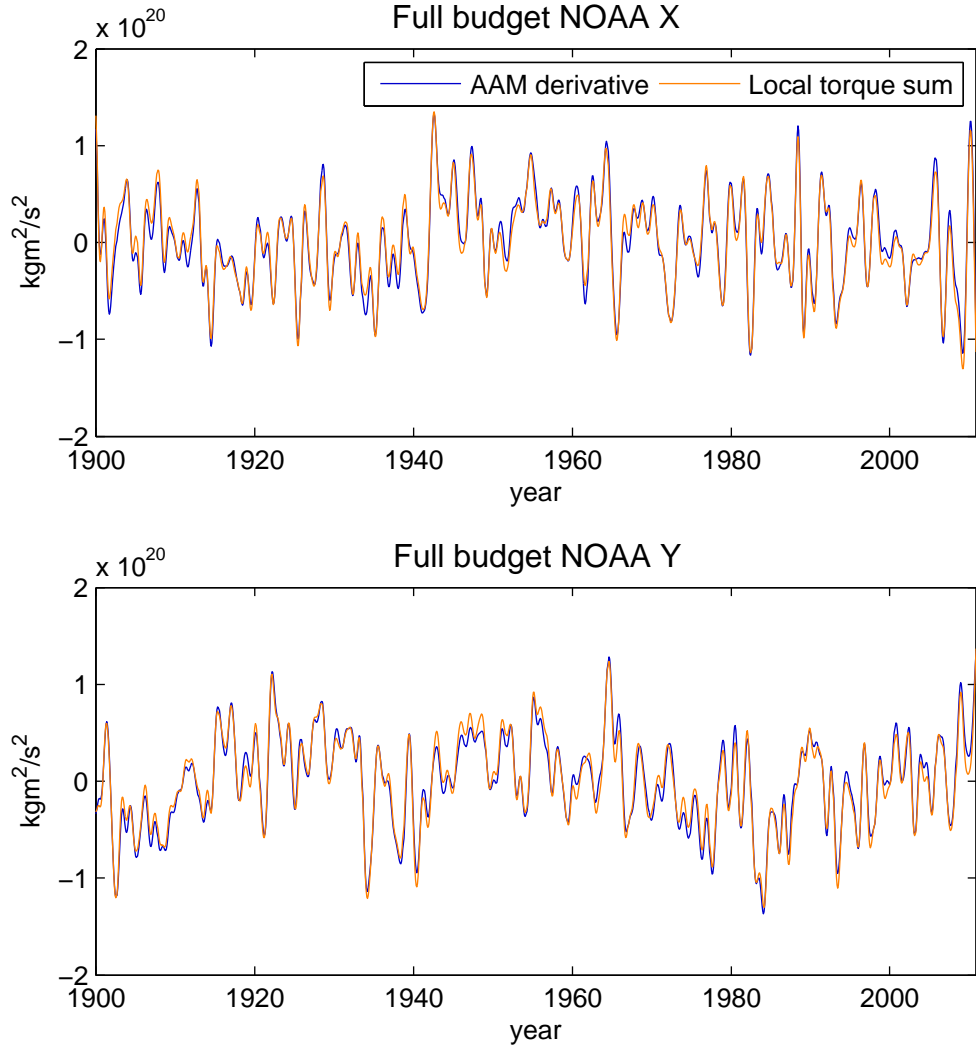


Figure 5.11: Full angular momentum budget of NOAA

Table 5.4: Standard deviation $[\frac{\text{kgm}^2}{\text{s}^2}]$ and correlation: Full AAM Budget

	σ_x	σ_y	C_x	C_y
ERA	5.86×10^{18}	6.38×10^{18}	0.99	0.99
NOAA	8.19×10^{18}	8.24×10^{18}	0.98	0.98

The visual and statistical comparison shows a nearly perfect match for

both models at all time periods. The correlation coefficients are ~ 1.0 and the standard deviations are virtually negligible compared to the amplitudes, see Table 5.4. Thus, the use of this budget analysis when judging the rational skill of the models is little. The main point in evaluating this version was more to get a complete picture of all possible AAM budget versions through this study.

Residual budget

The residual version of the AAM budget describes one of the key measures concerning the reliability of both reanalyses. The evaluation of this version uses a different low-pass filter than the one of the full budget. Instead of a cut-off frequency of 1.5 yr, 6 yr was chosen in order to prepare for a better judgement of decadal variations. The resulting time series can be seen in Figure 5.12 and 5.13.

Overall the time series of the residual budget show good agreement for both models throughout the whole century but they also give the first hint of the superiority of the ERA model. With higher correlation and a smaller standard deviation for both x - and y -component (Table 5.5) a clear decision pro ERA can be made for the first time. Another possible shortcoming within the NOAA series is the external computation of the surface stress used for the friction torque. For that reason, another version of the budget equation was numerically validated.

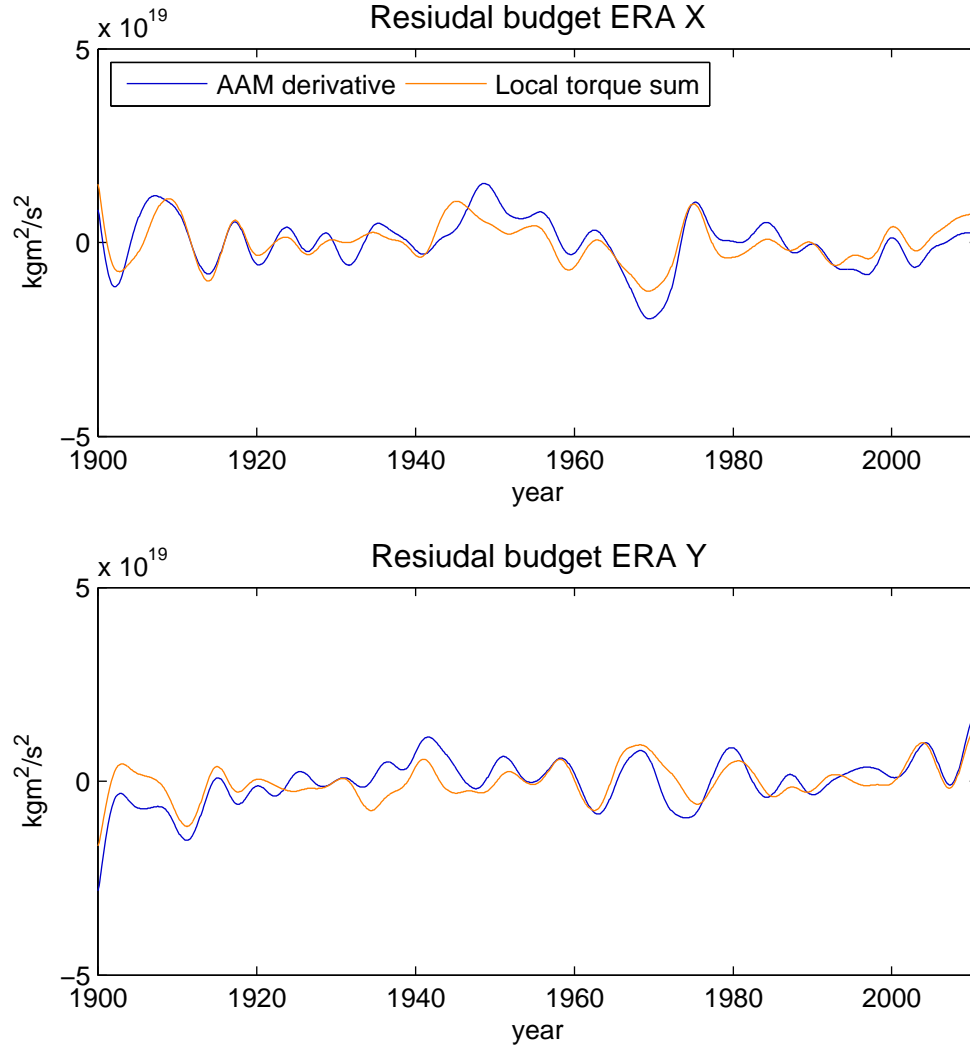


Figure 5.12: Residual angular momentum budget of ERA

Table 5.5: Standard deviation $[\frac{\text{kgm}^2}{\text{s}^2}]$ and correlation: Residual AAM Budget

	σ_x	σ_y	C_x	C_y
ERA	3.90×10^{18}	4.23×10^{18}	0.81	0.71
NOAA	5.93×10^{18}	6.40×10^{18}	0.39	0.47

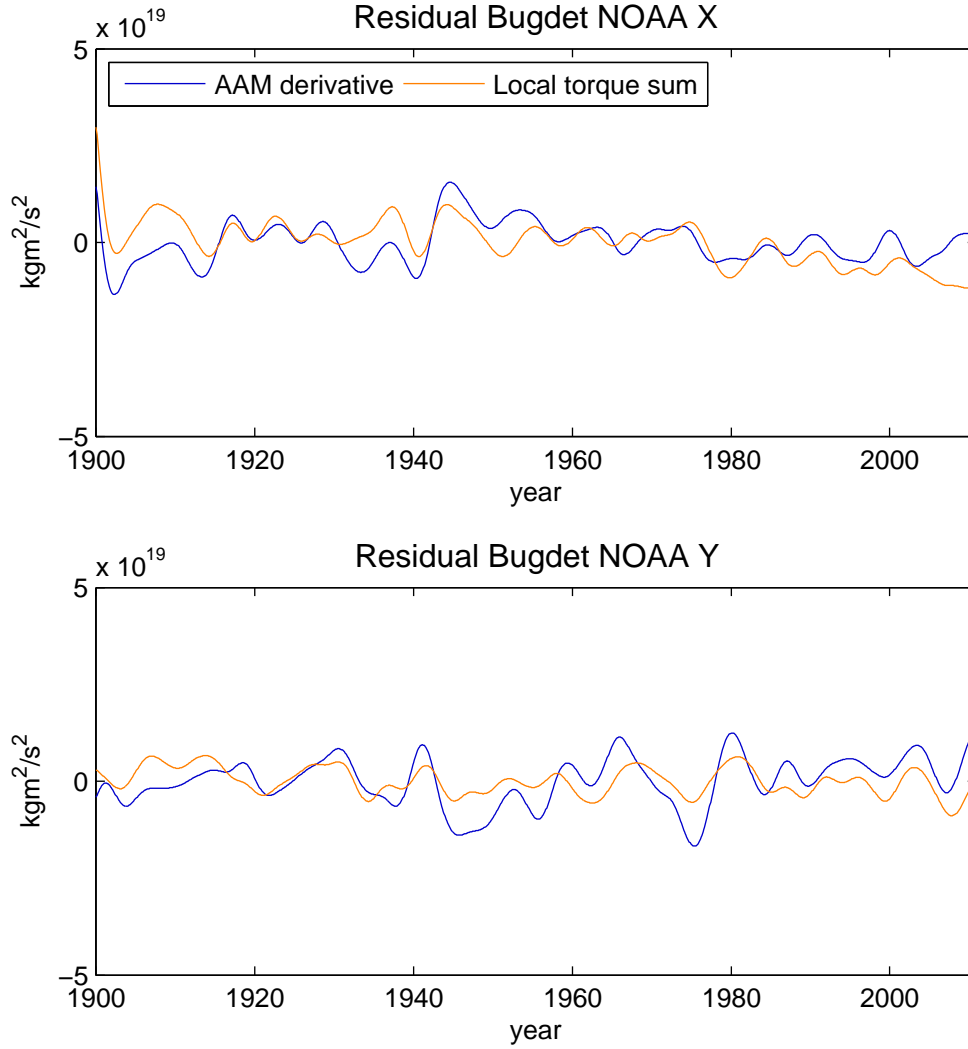


Figure 5.13: Residual angular momentum budget of NOAA

Wind term derivative versus mountain torque

The third version of the AAM budget compares the wind term derivative to the mountain torque. This is valid because of the rather small impact of the friction torque in the sum of the local components (Wahr, 1983 [28]). Considering this, and the fact that the pressure (ellipsoidal) terms have already been excluded in the residual budget, one might evaluate the budget

equation in form of (3.34).

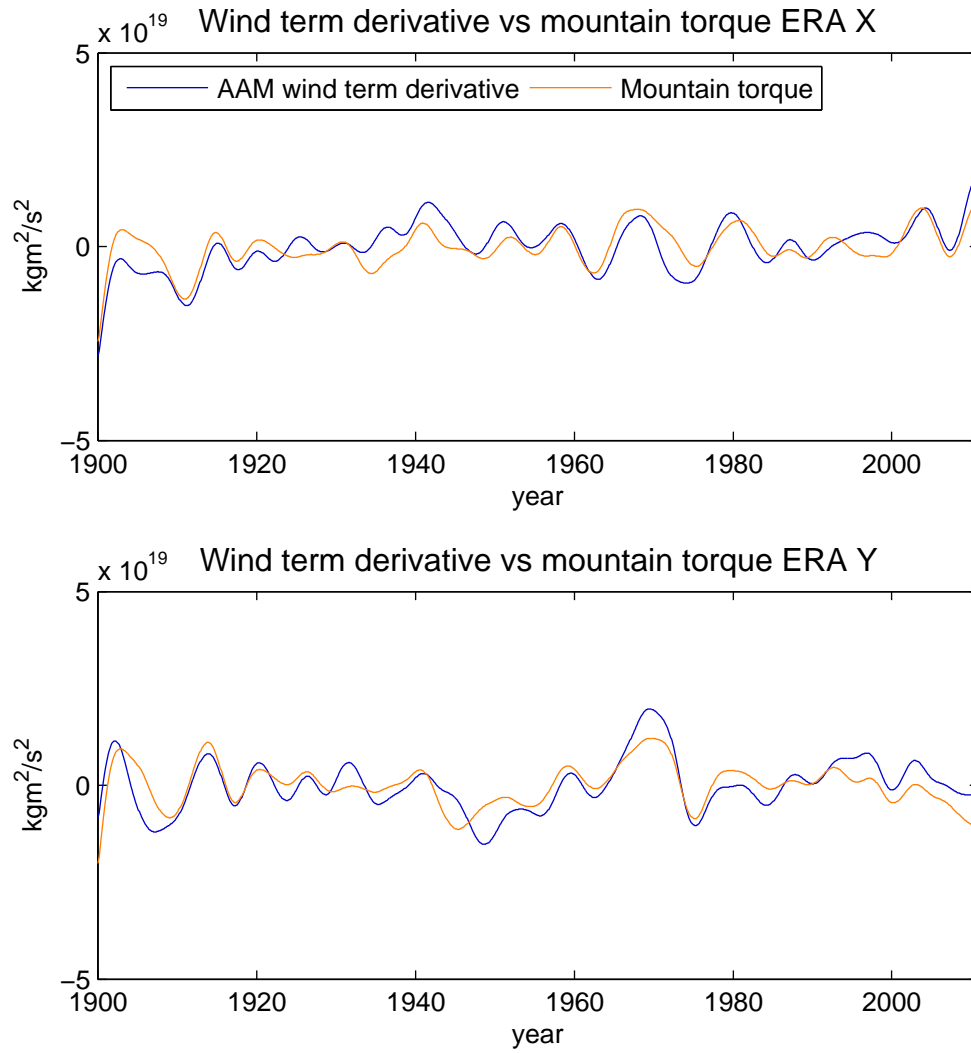


Figure 5.14: Wind term derivative versus mountain torque of ERA

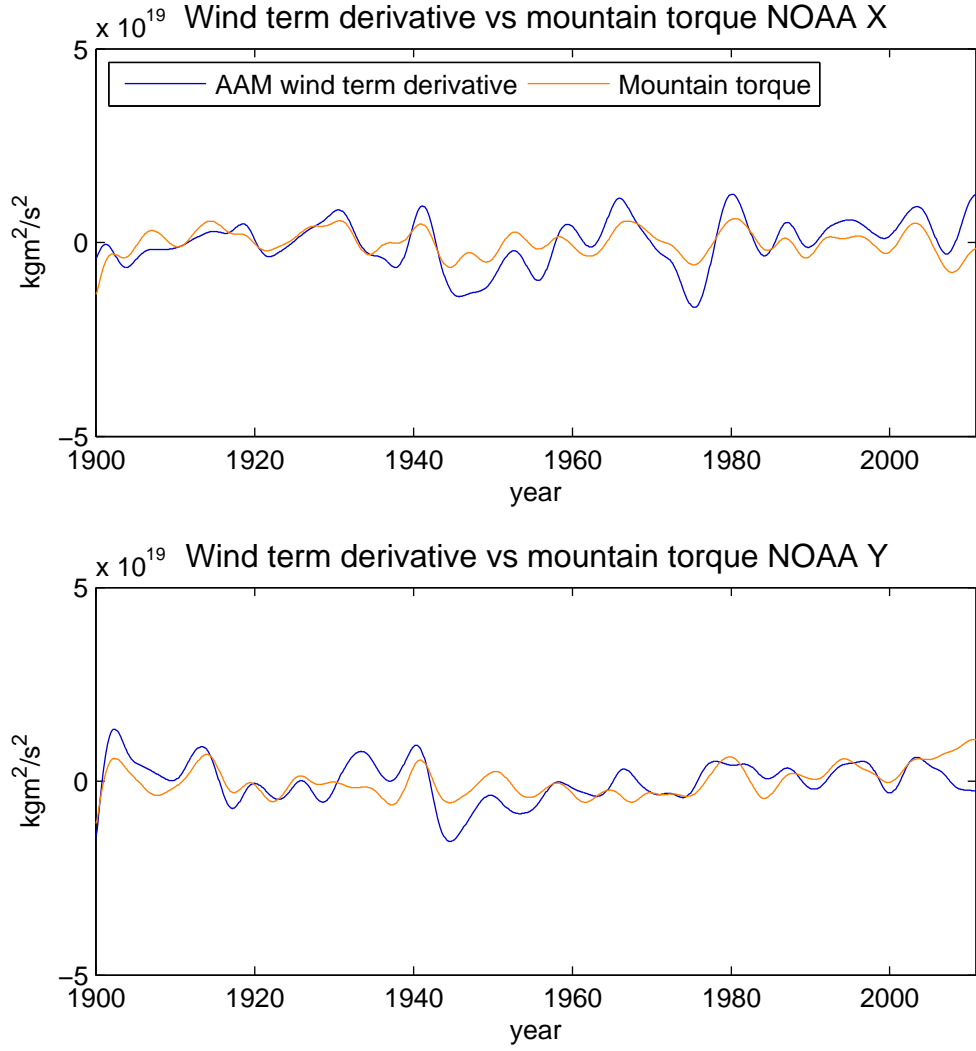


Figure 5.15: Wind term derivative versus mountain torque of NOAA

Table 5.6: Standard deviation $[\frac{\text{kgm}^2}{\text{s}^2}]$ and correlation: Wind term derivative vs mountain torque

	σ_x	σ_y	C_x	C_y
ERA	4.13×10^{18}	4.40×10^{18}	0.73	0.75
NOAA	4.66×10^{18}	4.55×10^{18}	0.67	0.52

These time series also show promising results over the whole analysis window in both cases. In general ERA provides the better results once again, but an interesting fact to consider is that the NOAA effort is much closer to the ERA results than it is for the residual budget. In other words, the inclusion of the friction torque weakens the results for NOAA. Although, like already mentioned above, the friction torque's impact is rather small, this can be seen as another prove for the problematic external evaluation of the surface stress. Compared to De Viron et al. (2004 [6]), the results for the residual budget of both models show better results than the Hadley centre data. This conclusion is derived only by visual comparison here since there are no values for correlation or standard deviation given in De Viron et al. (2004 [6]).

5.5.2 Frequency domain

The AAM budget should not only be investigated by visualizing time series and computing statistical measures but also by having a closer look at the signals in the frequency domain. Therefore two key measures were computed and plotted: squared coherence and phase lag following numerical recipes employed by Schindelegger et al. (2013 [25]). Both of them can be applied to the two parts of the budget equation and serve as an efficient tool in trying to give evidence about the reliability of the reanalysis models. This check in the frequency domain was applied to the residual budget only, because it is the most telling comparison.

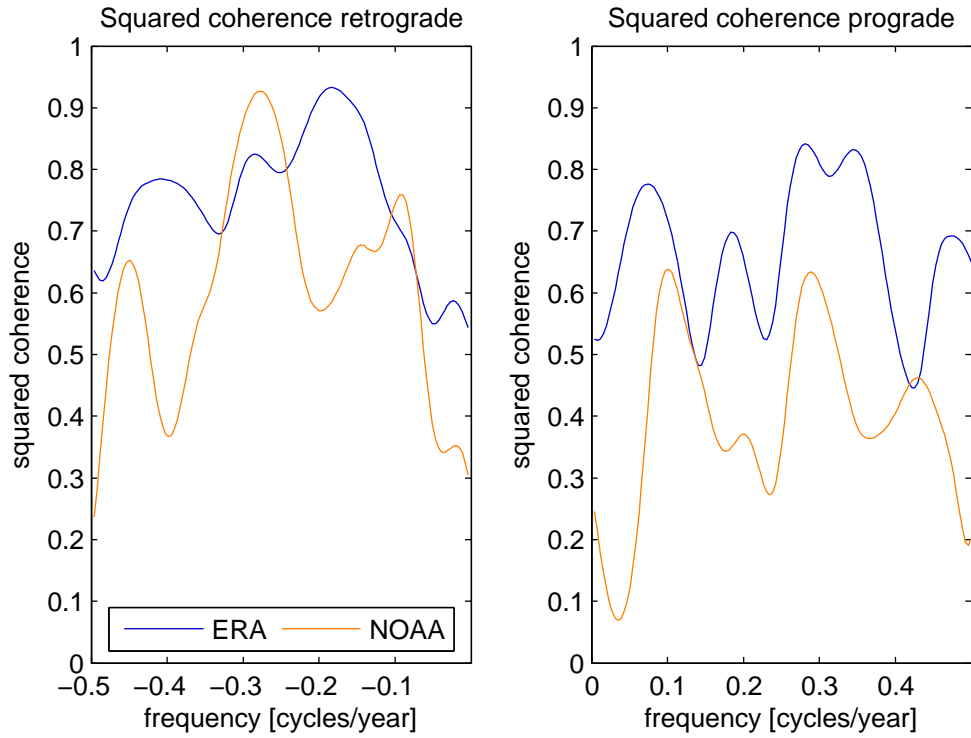


Figure 5.16: Squared coherence of the residual AAM budget

Figure 5.16 visualizes the fact that especially for ERA data the squared coherence is high for basically all frequencies shown in the plot. The NOAA data does not yield much weaker results either but, as before in the time domain, ERA proves its advantage. Of particular interest for this study are the frequencies < 0.1 cpy where ERA dominates the comparison even more than for shorter periods.

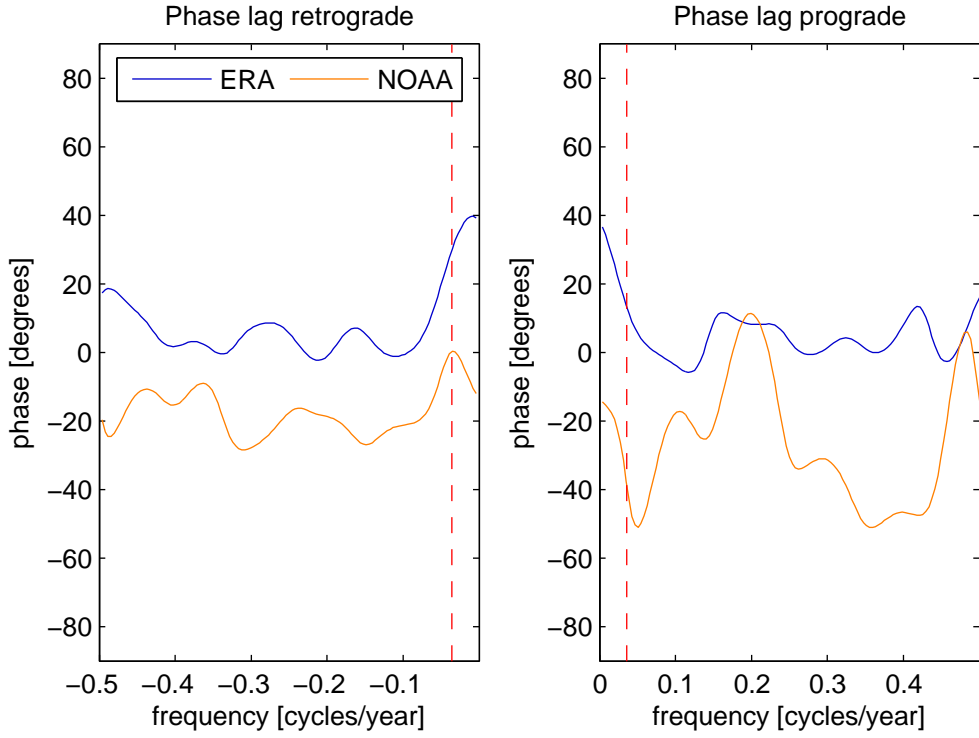


Figure 5.17: Phase lag of the residual AAM budget with frequency of Markowitz wobble (red)

A closer look at the phase lag of the residual budget (Figure 5.17) reveals an interesting fact. For the frequency of the Markowitz wobble (dashed red line) in the retrograde part the phase lag is ~ 0 , the ideal value which means that the signal parts of the torque sum and the AAM derivative are exactly in phase. At nearly all other frequencies ERA indicates to have the more stable and reliable balance in the budget but in this special (and here particularly important) case NOAA exhibits a better in-phase behaviour. Although this fact should not be overlooked, the combination of both measures, phase lag and squared coherence still testifies to the enhanced reliability of ERA.

5.6 Geophysical vs geodetic excitation

The final part of the practical implementation was the comparison of the excitation computed from meteorological data to those observed with geodetic and astrometric measurements. The approach for this task requires the computation of the so-called *geophysical excitation functions*, which then can be compared to the observed polar motion variations. All the calculations and visualisations in this chapter follow Gross et al. (2005 [12]).

5.6.1 Time domain

Geophysical excitation functions

In the first step the excitation functions $\hat{\chi}(t)$ were derived from equation (3.17). They were all computed using IB pressure terms. As already mentioned in Section 3.1, the numerical values for the evaluation of (3.17) were taken from Gross et al. (2007 [13]). $\hat{\chi}(t)$ in x - and y -direction are illustrated in Figure 5.18 and the standard deviation and correlation between ERA and NOAA are given in Table 5.7.

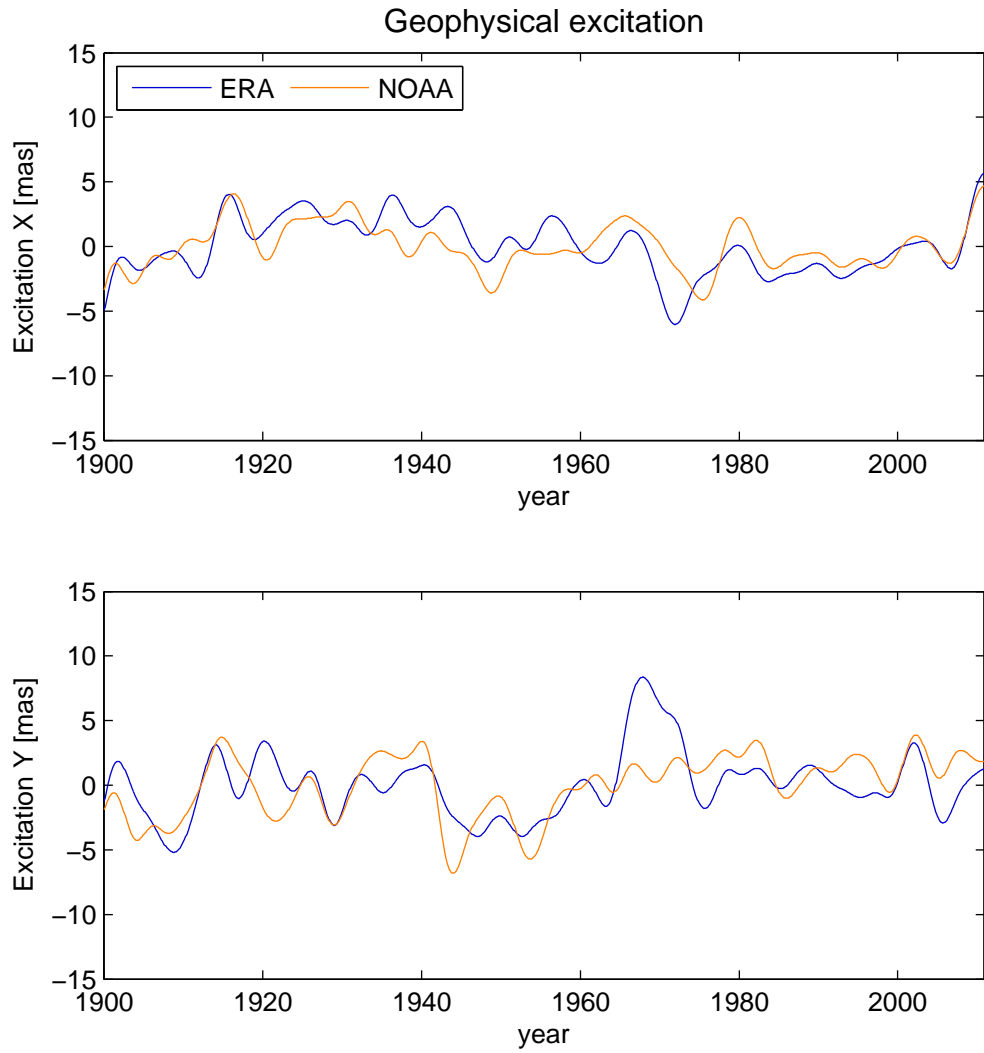


Figure 5.18: Geophysical excitation functions, detrended and low-pass filtered with 6 year cut-off

Table 5.7: Standard deviation [mas] and correlation: Geophysical excitation functions

	σ_x	σ_y	C_x	C_y
ERA/NOAA	1.65	2.39	0.65	0.54

Connection to geodetic observations

The excitation function $\chi(t)$, known as the polar motion excitation function, can be connected to $m(t)$ in complex notation through:

$$\hat{m}(t) + \frac{i}{\hat{\sigma}_0} \frac{d(t)}{dt} = \hat{\chi}(t) - \frac{i}{\Omega} \frac{d\hat{\chi}(t)}{dt} \quad (5.15)$$

where

$$\hat{m}(t) = m_x(t) + im_y(t), \quad (5.16)$$

being the direction cosines of the Earth's rotation axis relative to the axes of the rotating, body-fixed reference frame and

$$\hat{\sigma}_0 \equiv \frac{2\pi}{T_0} \left(1 + \frac{i}{2Q_0}\right) \quad (5.17)$$

is the complex frequency of the Chandler wobble with a period of T_0 and the resonance quality factor of Q_0 (Gross et al., 2005 [12]). Equation (5.15) connects changes in the equatorial part of the angular momentum with the location of the rotation pole. Since geodetic space techniques do not observe the rotation pole but the Celestial Intermediate Pole (CIP) in the rotating body-fixed frame, one has to rewrite (5.15) to:

$$\hat{p}(t) + \frac{i}{\hat{\sigma}_0} \frac{d\hat{p}(t)}{dt} = \hat{\chi}(t) \quad (5.18)$$

where

$$\hat{p}(t) = p_x(t) - ip_y(t). \quad (5.19)$$

Equation (5.18) describes the so-called *deconvolution*, the aim of which is to eliminate the Chandler wobble from the observed data. In order to secure a successful implementation of it, the resulting data was plotted in the frequency domain, showing the different periods contained in the signal. This is achieved using a Fast-Fourier Transformation (FFT) for the complex value $\hat{p}(t)$.

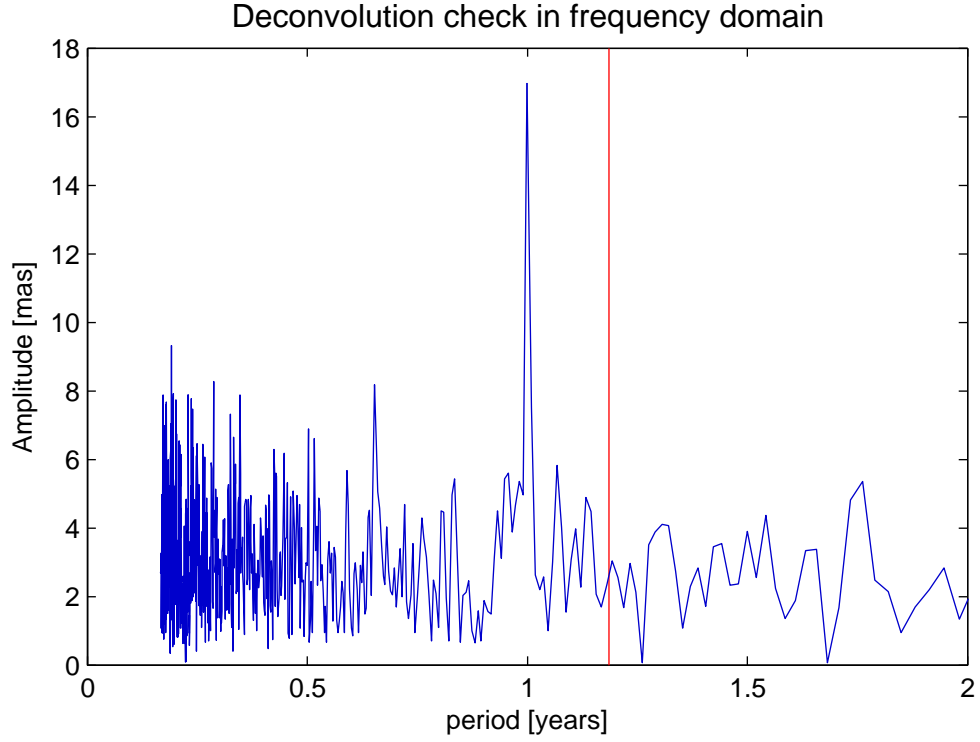


Figure 5.19: Check of the deconvolution in frequency domain using a FFT of the complex value $\hat{p}(t)$ (only prograde part shown here)

The visualization in Figure 5.19 confirms the fact that the Chandler wobble is fully filtered out of the data. The annual signal still exists as the peak at 1yr indicates. These time series for p_x and p_y were then filtered once again, using a cut-off frequency of 6 years in order to maintain longer periods only. The resulting filtered time series compared to the original data can be seen in Figure 5.20. As the Figure 5.20 indicates, all short periods ($< 5\text{--}6$ yr) vanished as a result of the filters and the deconvolution applied to the data.

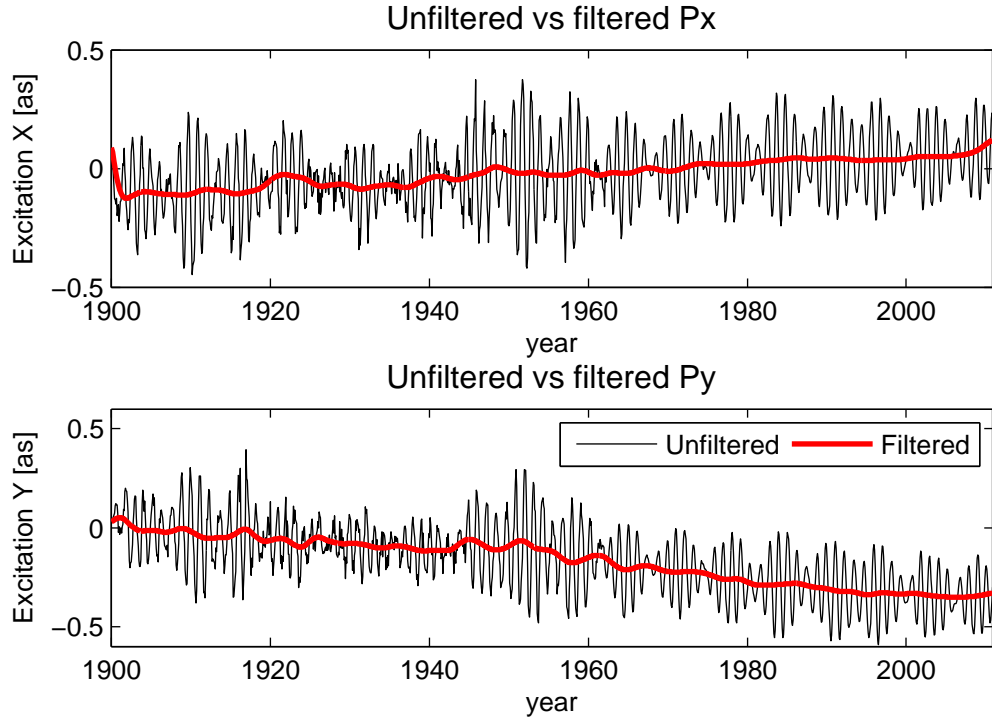


Figure 5.20: Comparison of unfiltered and filtered (6 years cut-off) data for p_x and p_y

Comparison of geodetic and geophysical excitation

The resulting time series could then be converted to [mas] and compared to the geophysical excitation functions of Figure 5.18. As expected from the outset of this study, the computed geophysical excitation can not account for a major part of the observed variations, neither in the x - nor in the y -component. This fact is also illustrated in Figure 5.21.

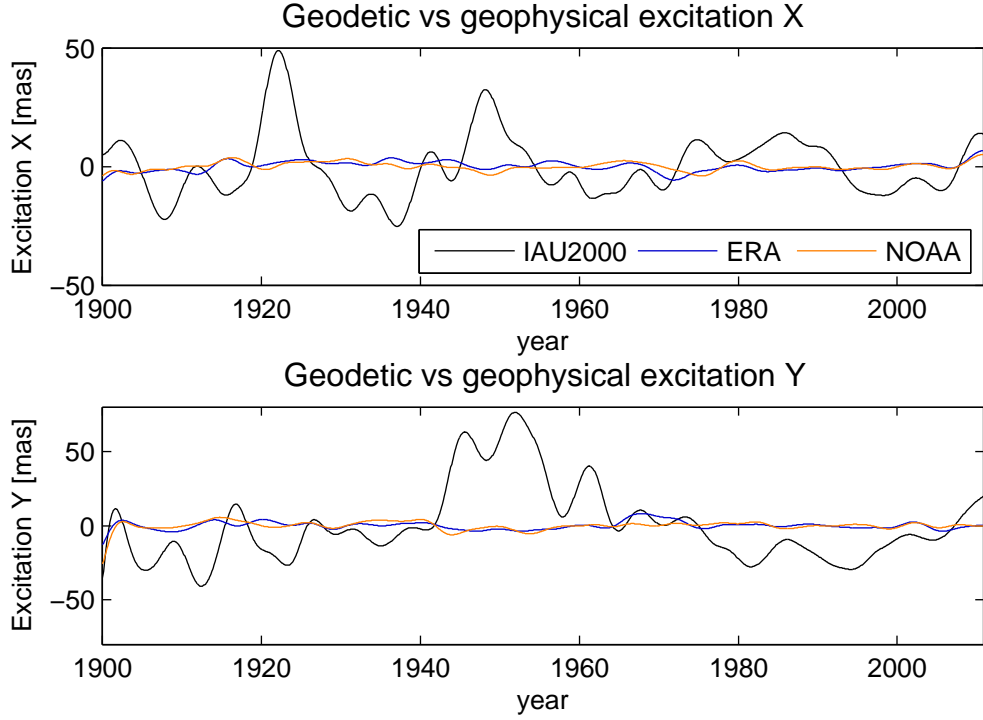


Figure 5.21: Comparison of geodetic and geophysical excitation, with all time series low-pass filtered using a 6-yr cut-off

Table 5.8: Peak-to-peak amplitudes [mas] for geophysical/geodetic excitation

	ERA	NOAA	IAU2000
1900-1950 (x/y)	8.99/17.24	7.68/31.89	120.7/153
1951-2010 (x/y)	11.70/12.33	8.84/9.61	110.3/273.4

To draw a comparison with the study of Gross et al. (2005, [12]), the peak-to-peak amplitudes were split into two periods: 1900 – 1950 and 1951 – 2010. The latter is the one that matches Gross et al.’s analysis window. It shows smaller results in x - and y -component for both models, accounting only for about 8% (x) and 4% (y) of the observed variations. The order of magnitude of the results is nearly equal for both models with the exception of the 1900–1950 period, where the excitation computed from NOAA shows significantly higher values than for ERA. Overall this study stays in

agreement with the fact that the atmospheric contribution to the observed decadal-scale wobbles is a rather small one.

5.6.2 Frequency domain

Similar to the check of the residual AAM budget in Section 5.5.2, the comparison of geophysical and geodetic excitation was also carried out in the frequency domain by visualizing squared coherence and phase lag values and splitting them into pro- and retrograde parts. The results are shown in Figures 5.22 and 5.23.

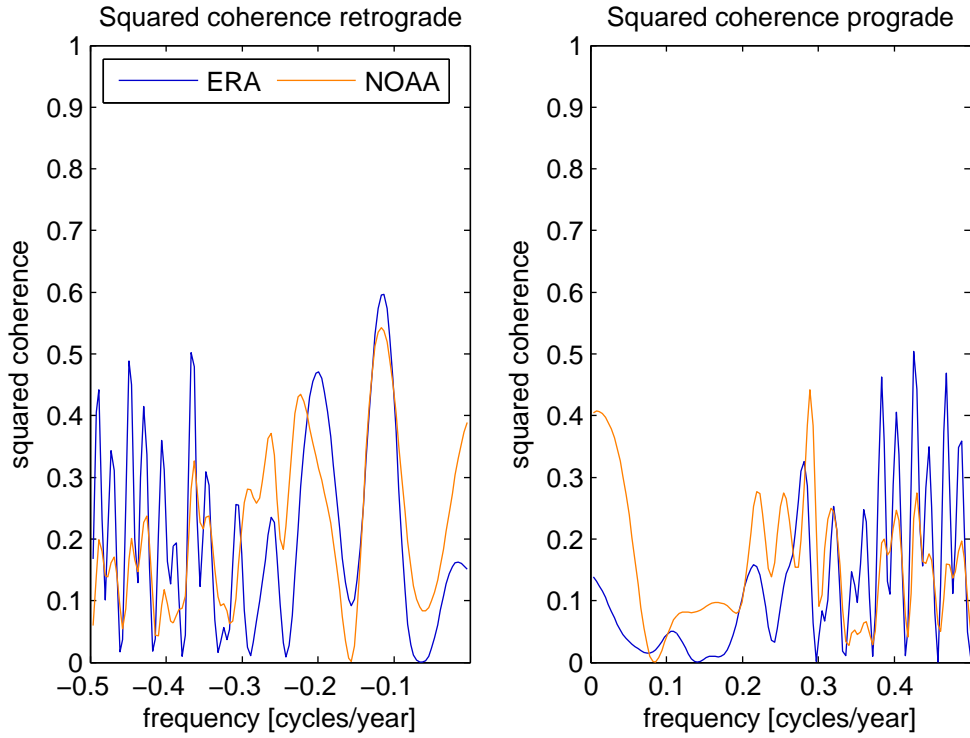


Figure 5.22: Squared coherence of the comparison: geophysical vs geodetic excitation

Figure 5.22 shows good results in the retrograde part for exactly decadal periods (0.1 cpy), where the squared coherence reaches up to ~ 0.6 for both ERA and NOAA. This is even higher than in Gross et al. (2005, [12]) where a value of ~ 0.4 was reached. Also included in the data is the 5 – 6 year oscillation that was pointed out before by de Viron et al. (2004, [6]). It can

be identified in the peaks at ± 0.2 - 0.3 cpy of the spectrum for ERA and NOAA.

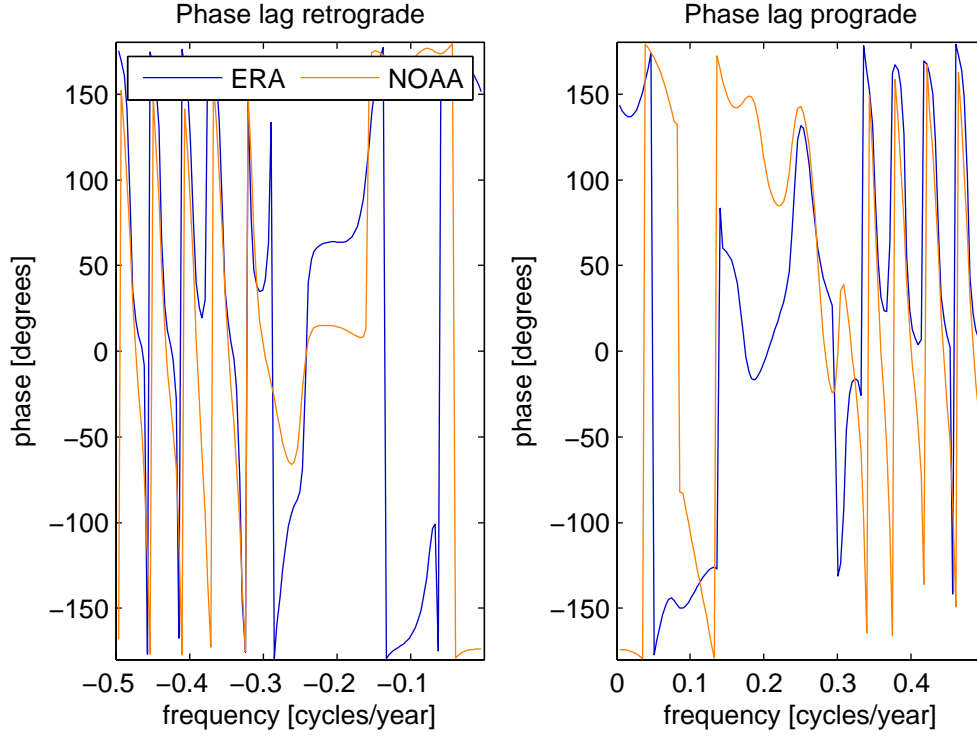


Figure 5.23: Phase lag of the comparison: geophysical vs geodetic excitation

The phase lag between the observed variations and those computed from the reanalysis data shows a likely out-of-phase behaviour for decadal periods including the Markowitz wobble band. This is in agreement with Gross et al. (2005, [12]), who obtained the same result with IB- ocean processes included. For the frequency band of the 5 – 6 year oscillation, both efforts produce near-zero values, indicating the relevance of atmosphere/ocean dynamics for this wobble signal.

Chapter 6

Discussion and final remarks

In the course of this thesis the atmospheric contribution to the decadal excitation of polar motion variations was investigated using meteorological data. The data was obtained from two separate reanalysis efforts that both span the whole twentieth century. Geophysical excitation measures were computed from it by applying the AAM approach for the atmospheric influence. This influence is a small one but the present results can still be a prerequisite for upcoming studies on this topic. In this closing remark the focus should be on the two main tasks of this study:

Estimation of the atmospheric influence

The atmospheric contribution turned out to be marginally significant as it could be expected from the knowledge of former studies. The computed geophysical excitation accounts only for a minor part of the observed one in both x - and y -component. Compared to the results of Gross et. al (2005, [12]) the atmosphere-induced peak-to-peak variations are even smaller, accounting only for $\sim 8\%$ (x) and 4% (y) of the observed variations. However, some portion of these inferior statistics might be due to the fact that Gross et al. used specially prepared EOP time series, which might be superior to C01. Both reanalysis models produce results of approximately the same order of magnitude, with the exception of the 1900-1951 period, where the NOAA values are significantly higher. In the frequency domain squared coherence and phase lag values were computed for both models, resulting in somewhat better results than those of Gross et. al (2005, [12]). The

squared coherence values are approximately 0.6–0.1 cpy but the phase lag shows a strong out-of-phase behaviour of both models for decadal periods. Additionally included in the data is a 5 – 6 year oscillation with a strong recognition factor, that was already pointed out before by De Viron et al. (2004, [6]).

Drawing a conclusion from all the facts mentioned above, it has to be stated that the contribution of the atmosphere can not account for a major part of decadal variations in the excitation of polar motion including the Markowitz wobble. This conjecture is based on the fact that the computed geophysical excitation is by far too small and that the computed and observed values are nearly entirely out of phase for decadal periods. The main processes driving decadal polar motion excitation are more likely found in the interior of the Earth, with interactions between the inner and outer core being the most promising candidates, see Section 2.3.1. In principle for studies like this one, the ocean response still has to be considered a major problem. For even more realistic results, a dynamic model for the response to pressure and wind forcing should be applied instead of the IB-approximation. Nevertheless the results of this thesis should serve as reliable estimates that may find consideration in future studies on this subject.

Test of the reanalysis models

The second major task of this study was the comparison of the ERA and NOAA reanalysis efforts and a judgement of their rational skill and reliability for usage in geodetic studies. Therefore a comparison of AAM and torque values and an evaluation of the AAM budget in three different versions were carried out. Overall, both models showed promising results in the respective budget checks but a superiority of the ERA data became apparent. Especially in the residual budget version ERA showed significantly better results, likely linked to the problematic external computation of the friction torque for NOAA. This fact can also be recognized in an improvement of NOAA in the third budget version, where the friction torque is left out of consideration. For the comparisons of ellipsoidal torque and wind term a third dataset, the NCEP/ NCAR reanalysis I from 1948 – 2009, was used as a benchmark for the other models. The correlations and standard deviations with it are of the same order of magnitude for both ERA and

NOAA. The results for both efforts are encouraging, indicating good consistency and endorsing the usability of the models for Earth rotation studies. ERA can be seen in a slightly superior position from a torque "perspective", mostly linked to the fact that NOAA does not provide surface stress values. The comparison with the Hadley centre data used by De Viron et al. (2004 [6]) shows the clear superiority of both ERA and NOAA, reaching better results for nearly all quantities investigated. The most unambiguous proof for that is given by the ellipsoidal torque series shown in Section 5.4.2.

List of Figures

2.1	Precession and nutation, Source: commons.wikimedia.org, accessed: July 2015	11
2.2	Polar motion from 1980–1998, Source: www.geodz.com, accessed: July 2015	12
3.1	Perturbations of the instantaneous rotation vector $\omega(t)$ with respect to π_{30} , the figure axis of an undeformed Earth. Source: Schindelegger et al. (2013 [24])	20
3.2	Illustration of angular momentum conservation (+/- arrows) in an Earth-fluid layer system as a pressure wave of two highs (orange areas) and two lows (blue areas) occurs in the atmosphere. Source: ggosatm.hg.tuwien.ac.at, accessed: July 2015	22
3.3	The different torque components, Source: Schindelegger et al. (2012 [23])	25
5.1	Manual calibration of the intersect parameter $b_{ocean} = 0.1$ (top) and $b_{land} = 0.06$ (bottom) in eastward direction. Label x -axis: $\sqrt{C_D}U$ (ocean) and $\sqrt{2C_D}U$ (land), y -axis: $\sqrt{\frac{\tau_E}{\rho_s}}$	35
5.2	Unfiltered mountain torque x -component time series from 1900 – 1925 computed from ERA-data	37
5.3	Mountain torque x -component time series from 1900 – 1925 computed from ERA data, low-pass filtered and with composite annual cycle removed	39
5.4	Comparison of a running average filter (red) to a common low-pass filter (blue) on NCEP AAM data: pressure term y -component	40
5.5	Comparison un-filtered vs filtered ellipsoidal torque NOAA x -component	41

5.6	Mountain torque computed for ERA and NOAA data. Both time series are filtered with a running average filter, detrended and with a seasonal cycle removed	43
5.7	Friction torque computed for ERA and NOAA data. Both time series are filtered with a running average filter, detrended and with a seasonal cycle removed	44
5.8	Ellipsoidal torque (non-IB) computed for ERA and NOAA data. Both time series are filtered with a running average filter, detrended and with a seasonal cycle removed	46
5.9	Wind term computed for ERA, NOAA and NCEP (1948 – 2009) data. The time series are filtered with a running average filter, detrended and with a seasonal cycle removed	47
5.10	Full angular momentum budget of ERA	50
5.11	Full angular momentum budget of NOAA	51
5.12	Residual angular momentum budget of ERA	53
5.13	Residual angular momentum budget of NOAA	54
5.14	Wind term derivative versus mountain torque of ERA	55
5.15	Wind term derivative versus mountain torque of NOAA	56
5.16	Squared coherence of the residual AAM budget	58
5.17	Phase lag of the residual AAM budget with frequency of Markowitz wobble (red)	59
5.18	Geophysical excitation functions, detrended and low-pass filtered with 6 year cut-off	61
5.19	Check of the deconvolution in frequency domain using a FFT of the complex value $\hat{p}(t)$ (only prograde part shown here)	63
5.20	Comparison of unfiltered and filtered (6 years cut-off) data for p_x and p_y	64
5.21	Comparison of geodetic and geophysical excitation, with all time series low-pass filtered using a 6-yr cut-off	65
5.22	Squared coherence of the comparison: geophysical vs geodetic excitation	66
5.23	Phase lag of the comparison: geophysical vs geodetic excitation	67

List of Tables

5.1	Standard deviation [$\frac{\text{kgm}^2}{\text{s}^2}$] and correlation for ERA/NOAA: Local torques	42
5.2	Standard deviation [$\frac{\text{kgm}^2}{\text{s}^2}$] (ellipsoidal torque) & $\frac{\text{kgm}^2}{\text{s}}$ (wind term)] and correlation ERA/NOAA: Ellipsoidal torque and wind term	48
5.3	Standard deviation [$\frac{\text{kgm}^2}{\text{s}^2}$] (ellipsoidal torque) & $\frac{\text{kgm}^2}{\text{s}}$ (wind term)] and correlation with NCEP series: Ellipsoidal torque and wind term	48
5.4	Standard deviation [$\frac{\text{kgm}^2}{\text{s}^2}$] and correlation: Full AAM Budget	51
5.5	Standard deviation [$\frac{\text{kgm}^2}{\text{s}^2}$] and correlation: Residual AAM Budget	53
5.6	Standard deviation [$\frac{\text{kgm}^2}{\text{s}^2}$] and correlation: Wind term deriva- tive vs mountain torque	56
5.7	Standard deviation [mas] and correlation: Geophysical exci- tation functions	61
5.8	Peak-to-peak amplitudes [mas] for geophysical/geodetic exci- tation	65

Acronyms

A, B	Equatorial moments of inertia
A'	$(A + B)/2$
A_{ocean}	Total ocean surface area
a	Mean Earth radius
b	Intersect parameter
C	Axial moment of inertia
C_D	Drag coefficient
C_m	Axial moment of inertia of crust and mantle
g	Mean gravitational acceleration
H	Angular momentum
$\hat{H}^{(a)}$	Atmospheric angular momentum
\hat{H}^p	Pressure term angular momentum
\hat{H}^w	Wind term angular momentum
\hat{h}	Relative angular momentum
h	Orthometric height, relative angular momentum (real part)
I	Tensor of inertia
$\Delta\hat{I}$	Deviation of tensor of inertia
i	Imaginary unit
J_2	Earth's form factor
L	Torque
\hat{L}^f	Friction torque
\hat{L}^g	Gravitational torque
\hat{L}^m	Mountain torque
$m_i, i = 1, 2, 3$	Perturbation of the rotation vector in the Tisserand system
\bar{p}_0	Mean pressure over ocean
p_{ocean}	Pressure distribution over ocean

p_s	Surface pressure
$(p_x \ p_y)$	Coordinates of CIP in the terrestrial reference system
Q_0	Resonance quality factor
T_0	Chandler period
U	Eastward ground-near wind velocity
u_*	Eastward friction velocity
V	Northward ground-near wind velocity
v_*	Northward friction velocity
θ	Co-latitude
λ	Longitude
$\hat{\sigma}_0$	Complex Chandler-frequency
σ_r	Euler-frequency
$\chi_i, i = 1, 2, 3$	Angular momentum functions
π_{30}	Figure axis of undeformed Earth
$\psi_i, i = 1, 2, 3$	Excitation functions
Ω	Constant mean angular velocity of the Earth
$\hat{\omega}$	Earth rotation vector
$\tau_\lambda, \tau_\theta$	East and south components of the friction force on the solid Earth

Bibliography

- [1] Barnes, R., Hide, R., White, A. and Wilson, C. (1983). Atmospheric angular momentum variations, length-of-day changes and polar motion. *Proc. R. Soc. Lond., A* 387, 31–73.
- [2] Bizouard C., Gambis D., The combined solution C04 for Earth Orientation Parameters consistent with International Terrestrial Reference Frame 2005. <http://hpiers.obspm.fr/eop-pc/>
- [3] Celaya, M.A., Wahr J.M., and Bryan F.O. (1999), Climate-driven polar motion, *J. Geophys. Res.*, 104, 12,813–12,829.
- [4] Compo, G.P. et al. (2011), The Twentieth Century Reanalysis Project, *Q.J.R Meteorol. Soc.* 137 1-28. DOI:10.1002/qj.776
- [5] de Viron, O., Bizouard C., Salstein D., Dehant V. (1999). Atmospheric torque on the Earth and comparison with atmospheric angular momentum variations, *J. Geophys. Res.*, 104 (B3), 4861-4875, 0148-0227/99/1998JB9000.
- [6] de Viron, O., Salstein D., Bizouard C., Fernandez L. (2004). Low-frequency excitation of length of day and polar motion by the atmosphere, *J. Geophys. Res.*, 109, B03408, 10.1029/2003JB002817
- [7] Dumberry, M., and Bloxham J. (2002), Inner core tilt and polar motion, *J. Geophys. Res.*, 151, 377–392.
- [8] Foreman, R.J., and Emeis S. (2010). Revisiting the Definition of the Drag Coefficient in the Marine Atmospheric Boundary Layer, *Journal Of Physical Oceanography*, 40, 10.1175/2010JPO4420.1.

- [9] Greiner-Mai, H., Jochmann H., and Barthelmes F. (2000) Influence of possible inner-core motions on the polar motion and the gravity field. *Phys. Earth Planet. Inter.*, 117, 81–93.
- [10] Greff-Lefftz, M., and Legros H. (1995), Core-mantle coupling and polar motion, *Phys. Earth Planet. Inter.*, 91, 273–283.
- [11] Gross, R.S., and Vondrak J. (1999), Astrometric and space-geodetic observations of polar wander, *Geophys. Res. Lett.*, 26, 2085–2088.
- [12] Gross, R.S., Fukumori I., Menemenlis D. (2005), Atmospheric and oceanic excitation of decadal-scale Earth orientation variations, *J. Geophys. Res.*, 110, B09405, 10.1029/2004JB003565.
- [13] Gross, R.S. (2007), Earth Roation Variations – Long Period, in *Physical Geodesy*, edited by T. A. Herring, *Treatise on Geophysics*, Vol. 11, Elsevier, Amsterdam.
- [14] Hellerman, S., and Rosenstein M. (1983), Normal Monthly Wind Stress Over the World Ocean with Error Estimates, *Journal Of Physical Oceanography*, 13.
- [15] Kalnay, E., et al. (1996), The NCEP/NCAR 40-year reanalysis project. *Bull. Amer. Meteor. Soc.*, 77, 437–471.
- [16] Markowitz, W. (1960), Latitude and longitude, and the secular motion of the pole, in *Methods and Techniques in Geophysics*, edited by S. K. Runcorn, pp. 325–361, Wiley-Interscience, Hoboken, N. J.
- [17] Meschede, D. (2004), *Gerthesen Physik*, 22. Auflage, Springer Verlag, Berlin-Heidelberg-New York.
- [18] Mound, J.E. (2005), Electromagnetic torques in the core and resonant excitation of decadal polar motion, *J. Geophys. Res.*, 160, 721–728 doi: 10.1111/j.1365-246X.2004.02495.
- [19] Munk, W. and MacDonald, G. (1960). *The Rotation of the Earth: A Geophysical Discussion*. Cambridge University Press, New York.
- [20] Poli P. et al. (2013), The data assimilation system and initial performance evaluation of the ECMWF pilot reanalysis of the 20th-century

assimilating surface observations only (ERA-20C), *Series: ERA Report Series*, European Centre for Medium-Range Weather Forecasts, Reading, UK.

- [21] Seitz, F. (2004), Atmosphärische und ozeanische Einüsse auf die Rotation der Erde: Numerische Untersuchungen mit einem dynamischen Erdsystemmodell. C578, Deutsche Geodätische Kommission, München (in German).
- [22] Schindelegger, M. (2009), Modellierung atmosphärischer Einflüsse auf die Erdrotation in verschiedenen Zeitskalen, Diplomarbeit, Institut für Geodäsie und Geophysik der Technischen Universität Wien.
- [23] Schindelegger, M., Böhm J., Schuh H., Salstein D. (2012) Modellierung von Erdrotationsschwankungen mittels atmosphärischer Drehmomente. Geodetic Week, 9-11 October 2012.
- [24] Schindelegger, M., Böhm S., Böhm J., Schuh H. (2013a), Atmospheric effects on Earth rotation, in Böhm J., Schuh H. (eds), *Atmospheric effects in Space geodesy*, Springer.
- [25] Schindelegger, M., Salstein D., Böhm J. (2013b), Recent estimates of Earth-atmosphere interaction torques and their use in studying polar motion variability, *J. Geophys. Res. Solid Earth*, 118, 4586–4598, doi:10.1002/jgrb.50322.
- [26] Schindelegger, M. (2014). Atmosphere-induced short period variations of Earth rotation, Dissertation, *Geowissenschaftliche Mitteilungen*, Heft Nr. 94, Veröffentlichung des Departments für Geodäsie und Geoinformation, ISSN 1811-8380.
- [27] Wahr, J. (1982). The effects of the atmosphere and oceans on the Earth's wobble and on the seasonal variations in the length of day - I. *Theory. Geophys. J. R. Astron. Soc.*, 74, 451–487.
- [28] Wahr, J. (1982). The effects of the atmosphere and oceans on the Earth's wobble and on the seasonal variations in the length of day - II. Results *Theory. Geophys. J. R. Astron. Soc.*, 70, 349–372.

- [29] Wilson, C.R. (1993), Contributions of water mass redistribution to polar motion excitation, in *Contributions of Space Geodesy to Geodynamics: Earth Dynamics, Geodyn. Ser.*, vol. 24, edited by D. E. Smith and D. L. Turcotte, pp. 77–82, AGU, Washington, D. C.